Memoirs of the Faculty of Science, Kyoto University, Series of Physics, Astrophysics, Geophysics and Chemistry, Vol. XXXV, No. 2 and 3, Article 2, 1979

STUDY ON THE REACTIONS $\gamma p \to \pi\pi N$ AND $\gamma p \to \pi \Delta$ IN THE ENERGY RANGE BETWEEN 710 MeV AND 950 MeV

By

Koichi MARUYAMA

Department of Physics, Faculty of Science, Kyoto University

(Received November 21, 1977)

ABSTRACT

Momentum spectra of photoproduced positive pions, negative pions, and recoil protons from hydrogen have been measured by a magnetic spectrometer at a laboratory angle of about 40°. A tagged photon beam in the energy range from 710 MeV to 950 MeV was used as the incident beam. The charged particles associated with the spectrometer particle detected by the magnetic spectrometer were also detected in coincidence by scintillation counter hodoscopes.

The cross sections of the processes $\gamma p \to \pi\pi N$ and $\gamma p \to \pi \Delta$ have been deduced from these measurements. Both cross sections of $\gamma p \to \pi^- \Delta^{++}$ and $\gamma p \to \pi^+ \Delta^0$ are well reproduced by the GIOPE model with s-channel resonances.

The behavior of the cross sections of $\gamma p \to \pi^0 \pi^0 p$ suggests a large contribution of s-channel resonances in the second resonance region.

TABLE OF CONTENTS

I. Introduction

Although there exist large amount of contributions from double pion photoproduction to the total photoproduction cross section from protons in the resonance region, experimental data of double pion photoproduction are very scarce in contrast with those of single pion photoproduction.[1)]

Among the following three reactions,

$$\gamma p \to \pi^- \pi^+ p, \tag{I–1}$$

$$\gamma p \to \pi^+ \pi^\circ n, \tag{I–2}$$

$$\gamma p \to \pi^\circ \pi^\circ p, \tag{I–3}$$

only the first process has been extensively studied experimentally[2~8)] and theoretically, and the results indicate that the reaction is dominated by the quasi-two body reaction

$$\gamma p \to \pi^- \Delta^{++}$$
$$\qquad\quad \lfloor\!\to \pi^+ p,$$

with a small contribution of the reaction

$$\gamma p \to \pi^+ \Delta^\circ$$
$$\qquad\quad \lfloor\!\to \pi^- p,$$

in the photon energy range below the threshold of rho meson production.

The total cross section of reaction (I–2) below 700 MeV have been measured by Costa *et al.*[9)] by detecting neutrons. Their results indicate that the size of cross section of reaction (I–2) is about the same as the one of reaction (I–1). Since they measured neutron alone in process (I–2), their analysis on the contribution of the quasi-two body reactions depends on the theoretical model.

Concerning reaction (I–3), the situation is worse than that of reaction (I–2). Although several experiments on reaction (I–3) have been performed[10,11)] the size and behavior of the cross sections have not been established well, and we have very poor knowledges on the reaction mechanism of the reaction from the existing data.

Here we restrict ourselves to the quasi-two body reactions,

$$\gamma p \to \pi^- \Delta^{++}, \quad \text{(I-4)}$$

$$\gamma p \to \pi^+ \Delta^0, \quad \text{(I-5)}$$

$$\gamma p \to \pi^0 \Delta^+. \quad \text{(I-6)}$$

The total cross section, the differential cross section, and the decay density matrix element of reaction (I-4) have been measured. The total cross section which rises rapidly from the threshold, has a maximum of about 70 μb at around 650 MeV, and then falls slowly as the photon energy increases. The differential cross section shows a forward peak which may suggest the pion exchange contribution to this process.

Only a few measurements on the total cross section and the differential cross section of reaction (I-5) have been performed. The Bubble Chamber experiments[2~4] showed very small total cross sections. On the other hand, the counter experiment[8] showed fairly large differential cross sections.

No measurement on reaction (I-6) has been done.

Three kinds of theoretical analyses on these quasi-two body reactions in the resonance region have been performed until now. The OPE (one pion exchange) model for charged pion processes proposed by Drell[12] was extended to the GIOPE (gauge invariant OPE) model by Stichel and Scholz.[13] The GIOPE model which included an absorptive correction for the $\pi N \Delta$ vertex to take account of the off-mass shell effect of the exchanged pion, was compared with the experimental data of $\gamma p \to \pi^- \Delta^{++}$ by ABBHHM group.[3] The results showed a qualitative agreement between the model and the experiment. The second analysis is the isobar model. CEA group proposed this model which contained the isobars $P_{11}(1420)$, $D_{13}(1512)$, $F_{15}(1688)$, and $F_{37}(1924)$ to explain their $\gamma p \to \pi^- \Delta^{++}$ data, and found a rough agreement of the model with their data.[2] The third one is the GIOPE model with the above isobars, or the combination of the former two models. Lüke *et al.*,[14] Ciocchetti *et al.*,[15] Lüke,[16] Zayats,[17] and Sasaki[18] analyzed the reaction $\gamma p \to \pi^- \Delta^{++}$ using this model. The last three authors analyzed also the reaction $\gamma p \to \pi^+ \Delta^0$ by this model. All of these analyses reproduced the experimental data qualitatively. But the amounts of the absorptive correction and that of the isobar contribution were not well determined from the experimental data.

In order to clarify the reaction mechanism of double pion photoproduction reactions (I-1), (I-2), and (I-3), and of quasi-two body reactions (I-4), (I-5), and (I-6) in the second resonance region, it is needed to supply the precise experimental data on these processes. We have performed an experiment to measure the accurate spectra of photoproduced negative pions, positive pions, and recoil protons from hydrogen in the photon energy range from 710 MeV to 950 MeV.

A general description of this experiment is given in Chapter II. The experimental apparatus is described in Chapter III. The method for the determination of the physical quantities and the procedure for the reconstruction of each event are given in Chapter IV. Chapter V describes the derivation of the cross section. The results are given and discussed in Chapter VI.

II. Experiment

II-1. General

As it is very difficult to determine the photon energy for studying double pion

photoproduction reactions with a usual bremsstrahlung beam. The present experiment has been performed using a photon tagging system of the 1.3 GeV electron synchrotron at the Institute for Nuclear Study, University of Tokyo. In this experiment a photon energy range from 710 MeV to 950 MeV has been covered at one setting of the energy of the incident electron beam. The photon energy range has been chosen to study double pion photoproduction in the second resonance region. The intensity of the tagged photon beam is restricted within an order of 10^5 γ/sec due to the counting speed of scintillation counters. So it is required to use detectors which have large acceptances for getting a sufficient yield within a proper machine time.

The tagged photon beam hit a liquid hydrogen target as shown in Fig. 1. The momenta of negative and positive pions and protons were measured with a magnetic spectrometer having an acceptance of about 20 msr. The magnetic field strengths of 2.5 kG and 5.0 kG have been chosen for pions and protons, respectively. The lowest measurable momenta by the spectrometer are about 100 MeV/c and 300 MeV/c for pions and protons, respectively. Although the spectrometer has an enough acceptance in the higher momentum region, the available highest momentum was 900 MeV/c for both of pions and protons. The spectrometer was set at a laboratory angle of about 40°.

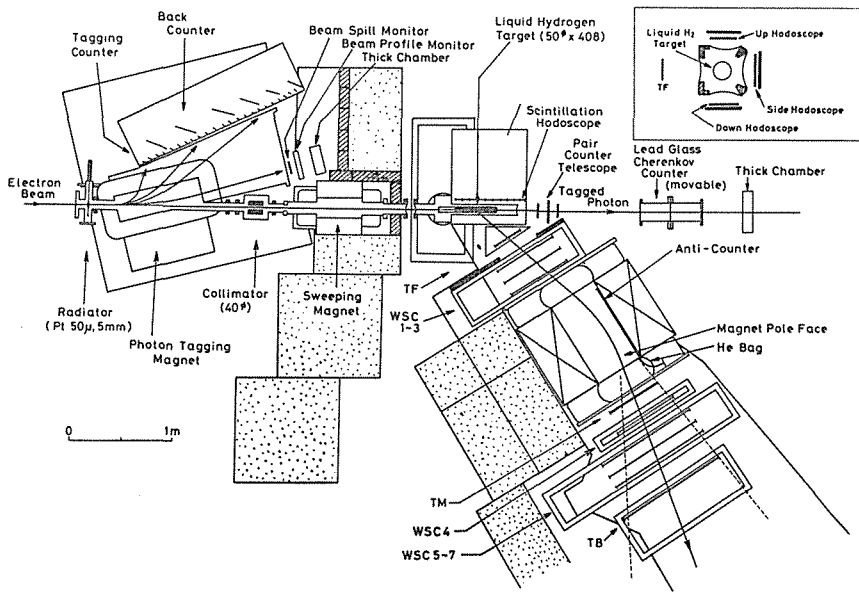

Fig. 1. Arrangement of the experimental apparatus.

To identify the particles, TOF (time-of-flight) between two scintillation counters in the spectrometer was measured.

In order to identify the reaction, charged particles in a missing particle(*) associating with the spectrometer particle(*) were detected by counter hodoscopes

(*) Hereafter we express the particles detected with the spectrometer as *the spectrometer particle* and the combination of other particles in the final state as *the missing particle*. For example, in the case of the reaction $\gamma p \to \pi_1 \pi_2 N$ π_1 is *the spectrometer particle* and ($\pi_2 N$) is *the missing particle*.

surrounding the liquid hydrogen target.

The kinematical regions of this experiment for pions and protons are illustrated in Fig. 2.

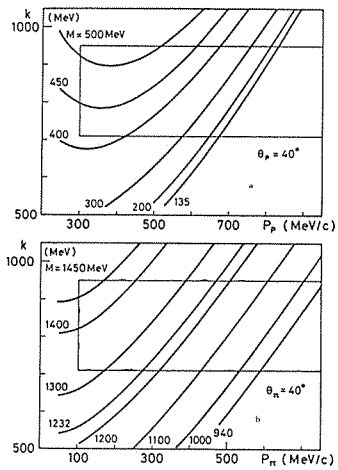

Figs. 2. Laboratory kinematics of the present experiment for the spectrometer particle at a laboratory angle of 40°. The smooth curves are lines of constant missing mass of the spectrometer particle. The blocks show the ranges covered in this experiment. (a) The spectrometer particles are protons. (b) The spectrometer particles are charged pions.

II-2. Measured Spectra

The spectra of the following seven kinds of reactions have been measured:

$$\gamma p \to \pi^- X^{++}, \tag{II-1}$$

$$\gamma p \to \pi^+ X^{\circ}, \tag{II-2}$$

$$\gamma p \to \pi^+ X^{+-}, \tag{II-3}$$

$$\gamma p \to \pi^+ X^{\circ\circ}, \tag{II-4}$$

$$\gamma p \to p X^{\circ}, \tag{II-5}$$

$$\gamma p \to p X^{+-}, \tag{II-6}$$

$$\gamma p \to p X^{\circ\circ}, \tag{II-7}$$

where wa use the abbreviations for the missing particles:

X^{++}; two positive particles are contained at least and the sum of charges of all particles is plus two,

X° ; the sum of all charges is zero,

X^{+-}; one positive particle and one negative particle are contained at least and the sum of charges is zero,

$X^{\circ\circ}$; all particles are neutral.

X^{++}, X°, X^{+-}, and $X^{\circ\circ}$ are any resonant or nonresonant hadronic final states which are not detected by the spectrometer. These final states are described by an invariant mass M, which was experimentally determined by the missing mass technique. The

sum of reactions (II–3) and (II–4) is equal to reaction (II–2) and the sum of reactions (II–6) and (II–7) is equal to reaction (II–5). Possible combinations of particles in the final state of these reactions are listed in Table 1.

Table 1. List of the combinations of particles in the final states.

Final State	Combination of Particles		
	2-body	3-body	4-body
π^-X^{++}	No	$\pi^-(\pi^+p)$	$\pi^-(\pi^\circ\pi^+p)$ $\pi^-(\pi^+\pi^+n)$
π^+X°	π^+n	$\pi^+(\pi^-p)$ $\pi^+(\pi^\circ n)$	$\pi^+(\pi^-\pi^\circ p)$ $\pi^+(\pi^-\pi^+n)$ $\pi^+(\pi^\circ\pi^\circ n)$
π^+X^{+-}	No	$\pi^+(\pi^-p)$	$\pi^+(\pi^-\pi^\circ p)$ $\pi^+(\pi^-\pi^+n)$
$\pi^+X^{\circ\circ}$	π^+n	$\pi^+(\pi^\circ n)$	$\pi^+(\pi^\circ\pi^\circ n)$
pX°	$p\pi^\circ$	$p(\pi^-\pi^+)$	$p(\pi^-\pi^\circ\pi^+)$
pX^{+-}	No	$p(\pi^\circ\pi^\circ)$ $p(\pi^-\pi^+)$	$p(\pi^\circ\pi^\circ\pi^\circ)$ $p(\pi^-\pi^\circ\pi^+)$
$pX^{\circ\circ}$	$p\pi^\circ$	$p(\pi^\circ\pi^\circ)$	$p(\pi^\circ\pi^\circ\pi^\circ)$

III. Experimental Apparatus

III-1. Tagged Photon Beam

(1) *Electron beam*

An electron beam was extracted from the 1.3 GeV electron synchrotron by using the one-third resonance method, and was transported to the experimental area through two bending magnets and a pair of quadrupole magnets. A 1 mm wide slit was set before the first bending magnet to get a smaller beam size, and a 5 mm wide slit was located before the second bending magnet to get a narrow momentum spread. The extracted electron beam had a momentum resolution of $\pm 0.3\%$ and had a spot size of 10 mmϕ at the position of the photon radiator in the photon tagging system. The energy of the electron beam was determined by the current of the synchrotron magnet, which was calibrated in advance by pair spectrometry within an error of 1%.

In order to monitor the spatial distribution of the electron beam throughout the experiment, a beam profile monitor of multiwire proportional chamber-type was located before a thick-walled ionization chember which served as an intensity monitor of the electron beam. The intensity of the electron beam was kept at around 10^8 e/s. The synchrotron was operated at low intensity to reduce the background associating with the electron beam.

(2) *Photon tagging system*[19]

The energies of photons which were emitted by electrons hitting the photon radiator were determined from the measurement of the energies of recoil electrons. The recoil electrons in the bremsstrahlung process were analyzed in momentum by the magnet and the tagging hodoscope.

A thin platinum foil of 5 mm in width and 30 mm in height was placed at the entrance of the tagging magnet as the photon radiator. The thickness of the radiator

was chosen to optimize the following two conditions; (a) the thinner radiator in the radiation length is desirable to reduce angular spread of recoil electrons, (b) the thicker one in the radiation length is desirable to get a higher conversion rate. The thickness of 50 μm (1.8×10^{-2} r.*l.*) was chosen. The conversion efficiency of electrons into the tagged photons was calculated to be about 5×10^{-3} photons/incident electron.

The magnet with a pole face of rectangular shape 770×210 mm^2 was used as an analyzing magnet, and the gap was 50 mm. The field strength of 11.7 kG was used. Details of the magnet construction, its field measurement, and the calculation of the trajectories were given elsewhere.[20]

A tagging hodoscope consisted of twenty five plastic scintillation counters were placed along the focal line of the magnet. Six back counters were used in coincidence with the tagging counters to eliminate the background which did not originated in the photon radiator. The width of the tagging counter varied from 31.8 mm for 105 MeV/c to 18.7 mm for 345 MeV/c to get a uniform momentum acceptance of 10 MeV/c. Each tagging counter made of a Pilot-B plastic scinitllator and viewed by an RCA–4517 photomultiplier supplied an output pulse of 3 ns in rise time and $6 \sim 7$ ns in width with 2 ns clipping line.

(3) *Tagged photon beam*

By setting the energy of the extracted electron beam at 1050 MeV, a tagged photon beam in the energy range from 710 MeV to 950 MeV was used in this experiment.

A photon beam from the photon tagging system had a spot size of 12 mmϕ at the position of the liquid hydrogen target 350 cm downstream from the radiator. The angular spread of the beam was less than ± 0.5 mrad. In order to eliminate a halo of the photon beam, a collimator made of lead and a sweeping magnet were located before the hydrogen target.

The performance of the photon tagging system was tested using a lead glass Cherenkov counter of total absorption type. The tagged photons were detected by the Cherenkov counter in coincidence with recoil electrons. The number of the tagged photons was counted by the coincidence between the signal from the tagging hodoscope $T_1, \ldots, T_{24}$, and that from the Cherenkov counter C, i.e., $T_1 \cdot C, \ldots, T_{24} \cdot C$.

At first we studied a relation between energy of the tagged photons and the numbers of the tagging channel. The peak channel of the pulse height spectrum of the Cherenkov counter gated by typical tagging counter is plotted in Fig. 3. There is a good linear relation.

A part of electrons detected by the tagging hodoscope did not accompany any photons. There were two sources of such electrons. One was the low energy electron background in the incident electron beam and the other was due to the second order process in the radiator. The former background was measured in the radiator-out run. Fig. 4 shows radiator-out to radiator-in ratios of recoil electron for each tagging counter. As the ratio increased to about $10\% \sim 20\%$ when the electron beam was not in good condition, we monitored the ratio throughout the experiment. The ratio was kept into about $1 \sim 2\%$ in the present experiment. After the radiator-out contribution was corrected, $7 \sim 10\%$ of recoil electrons did not accompany photons. The ratios,

$$\eta_i = \frac{T_i \cdot C}{T_i}, \qquad (i = 1, 24)$$

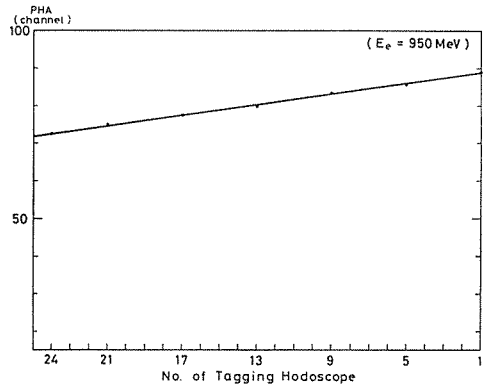

Fig. 3. Peak value of the Cherencov counter spectrum vs. the number of the tagging channel.

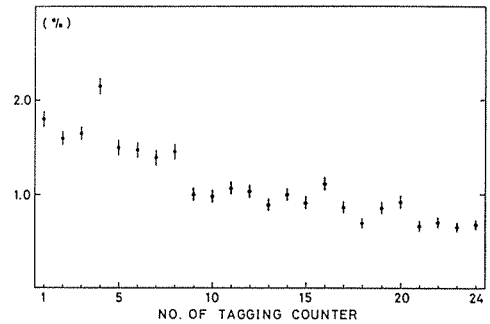

Fig. 4. Ratio of the counting rate of radiator-out to radiator-in for each tagging counter.

were shown in Fig. 5. The differences of η_i from 1.0 were considered to due to the contribution from the latter source. By a rough estimation of the second order processes, the trident production was the leading one. Total cross sections of this process was calculated to be 1.5 barn at 1050 MeV by the formula given by Block *et al.*[21] This value was comfortable to explain the above difference, however, there might be also a small contribution from the multiple process in the radiator.

The designed energy resolution of ± 5 MeV was worsened due to the following effects;

(a) finite size and angular divergence of the incident electron beam,

(b) multiple Coulomb scattering of incident and recoil electrons in the radiator.

A Monte Carlo calculation was performed to estimate the contribution from these effects, and the final energy resolution amounted to be about ± 7 MeV.

During the experiment the intensity of the tagged photon beam was kept to be less than 2×10^5/s for negative polarity run and 0.8×10^5/s for positive polarity run to keep the accidental coincidence rate between the tagging counters and the triggering counters less than 25%.

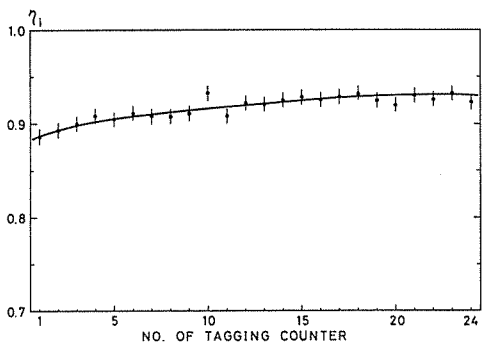

Fig. 5. The ratio η_i for each tagging counter.

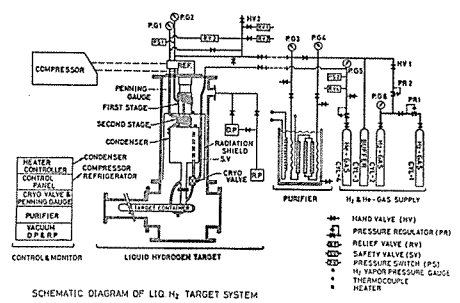

Fig. 6. Schematic diagram of the liquid hydrogen target system.

III-2. Liquid Hydrogen Target[22)]

Fig. 6 shows the construction of the liquid hydrogen target. Hydrogen gas was liquefied in the condenser attached to the Cryodine helium refrigerator (Model 1023). Liquid hydrogen transferred between the condenser and the target container through a cryo-valve. The target container was made of Mylar film of 127 μm thick, and had a cylindrical shape of 60 mm in diameter and 417 mm in length along the beam line. The temperature of liquid hydrogen was controlled within 0.2°K by the vapor pressure monitor.

The changes in the number of target hydrogen due to the contraction of the container at 20.4°K and the effect of the bubbles by boiling was less than $\pm 1\%$.

In order to reduce the energy loss of charged particles in the target and to reduce the conversion efficiency of photons as much as possible, we had designed a special vacuum jacket having the Mylar windows of 178 μm thick.

III-3. Magnetic Spectrometer

A magnetic spectrometer was used to determine four momentum of pions and protons. The spectrometer consisted of three set of triggering counters (TF, TM, and TB), a bending magnet, and seven planes of wire spark chambers (WSC 1~7). A helium bag was used to reduce the multiple Coulomb scattering.

(1) *Triggering counter*

Each of TF and TM consisted of two scintillation counters, and TB consisted of five scintillation counters. Dimensions of TF, TM, and TB are listed in Table 2. A three fold coincidence TF · TM · TB was used to trigger wire spark chambers.

Table 2. Specification of counters

Name		Size (mm^3) (vertical × horizontal × thickness)	Photomultiplior
Triggering Counters			
TF	TF1	58 × 132.5 × 2	RCA 8575
	TF2	58 × 160 × 2	:
TM	TM1	280 × 280 × 3	56 AVP
	TM2	280 × 280 × 3	:
TB	TB1	440 × 225 × 6	:
	TB2	440 × 225 × 6	:
	TB3	440 × 225 × 6	:
	TB4	440 × 225 × 6	:
	TB5	440 × 180 × 6	:
Charged Particle Hodoscope			
S1~S10		120 × 70 × 6	56 AVP
D1~D5		120 × 140 × 6	:
U1~U5		120 × 140 × 6	:
Backing Counter		120 × 350 × 13	:

(2) *Magnet*

The magnet with pole face of rectangular shape 860 × 500 mm^2 and with the gap of 250 mm was used to analyze the momenta. The measurement of the magnetic field in the median plane of this magnet was carried out by using an NMR probe as

a function of the exciting current. The field map was made at the central field strength of 2.5 kG and 5 kG by a rotating coil fluxmeter, which had been calibrated with the NMR system. Field distributions in the horizontal planes are shown in Fig. 7. The effective length of the magnetic field was determined to be 101.6 cm in the median plane. Although the field distributions depended on the vertical positions as seen in Fig. 7, the effective length was constant within $\pm 0.3\%$.

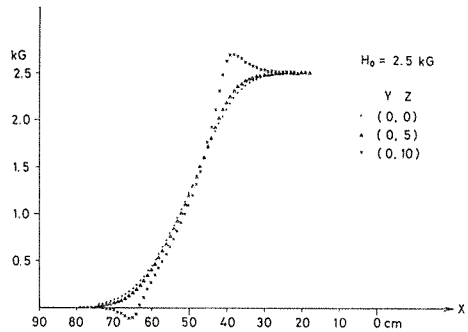

Fig. 7. Magnetic field distribution of the magnet in the horizontal planes at a central magnetic field strength of 2.5 kG; in the median plane (closed circles), in the plane 5 cm above the median plane (triangles), and in the plane 10 cm above the median plane (crosses).

(3) *Wire spark chamber*

The spatial coordinates of a particle passing through the spectrometer were measured by wire spark chambers with the magnetostrictive read out. Three chambers (WSC 1~3) were placed in the upstream side of the magnet and the other four (WSC 4~7) in the downstream side.

Dimensions of each chamber were listed in Table 3. The details of the construction and the performance were described in Appendix A.

Table 3. Specification of wire spark chambers. δ; angle between the direction of y-wires and the direction perpendicular to x-wires.
L_x; distance between the two fiducial wires in the x direction.
L_y; distance between the two fiducial wires in the y direction.

Name	Effective Area (mm^2) (horizontal × vertical)	δ	L_x (mm)	L_y (mm)	Distance from Target (cm)
1	650 × 370	−10°	950.8	580.3	61.5
2	:	10°	950.8	580.4	74.6
3	:	0°	949.6	600.3	88.0
4	:	0°	919.7	584.8	255.0
5	1040 × 660	0°	1479.3	909.8	275.9
6	:	10°	1481.4	900.0	287.0
7	:	−10°	1480.6	899.8	297.9

III-4. Charged Particle Hodoscope

As shown in Fig. 8, in order to detect charged particle from the target in coincidence with the spectrometer particle, three set of scintillation counter hodoscopes

were placed surrounding the hydrogen target. The side hodoscope consisted of ten scintillation counters (S1,..., S10), and each of the up and down hodoscopes consisted of five scintillation counters (U1,..., U5, and D1,..., D5). Two back counters were used in coincidence with each hodoscope to reduce background countings. Dimensions of each counter are listed in Table 2.

These hodoscopes were placed at 10 cm apart from the beam line. The resultant angular acceptance in θ as a function of the reaction point in the hydrogen target is shown in Fig. 9, where θ is an emission angle measured from the incident beam

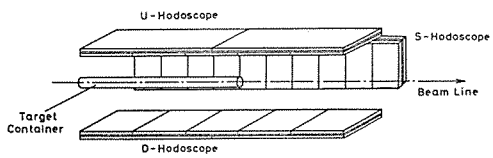

Fig. 8. A schematic drawing of the counter arrays of the charged particle hodoscopes.

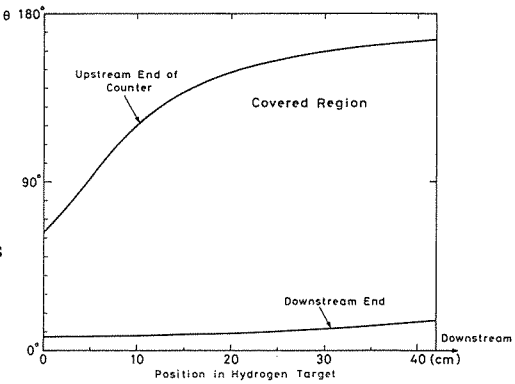

Fig. 9. Angular acceptance of the charged particle hodoscopes in θ as a function of the reaction point in the hydrogen target.

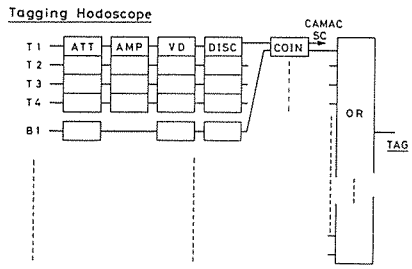

Fig. 10-a

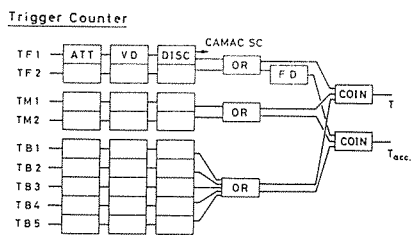

Fig. 10-b

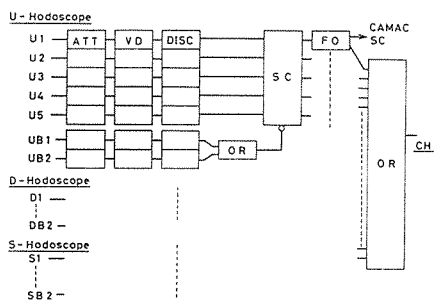

Fig. 10-c

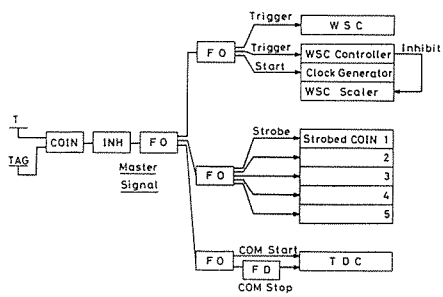

Fig. 10-d

Figs. 10. Simplified block diagram of the electronics. The notations are as follows: ATT, attenuator; AMP, amplifier; VD, variable delay; DISC, discriminator; COIN, coincidence; FD, fixed delay; SC, strobed coincidence; FO, fan-out; INH, inhibitor.

direction. The angular acceptance in ϕ, an angle in a plane normal to the beam line, was about 120°.

III-5. Electronics

Block diagrams of electronics used in this experiment are shown in Figs. 10. Coincidence signals between a tagging counter and the corresponding back counter, i.e., $T_1,\ldots, T_{24}$, were added together to give a main signal from the tagging system, TAG. The three fold coincidence signal of TF, TM, and TB i.e. T indicated the passage of a particle through the spectrometer. The signal of T or a two-fold coincidence signal of T·TAG was used as a master triggering signal.

The master signal played the following roles;

(1) to trigger a high voltage pulser for wire spark chambers,
(2) to open the gate of the read out circuits for wire spark chambers,
(3) to start a CAMAC time-to-digital convertor,
(4) to strobe CAMAC strobed coincidence modules.

After the triggering, the next master signal was inhibited about 300 ms for the data acquisition time by CAMAC-computer system and the recovery time of the high voltage power supply for wire spark chambers.

III-6. On-Line Data Taking

A data acquisition system is shown in Fig. 11. Data in the CAMAC modules were transferred to TOSBAC–40C computer through crate controllers of type A and a CAMAC branch driver.

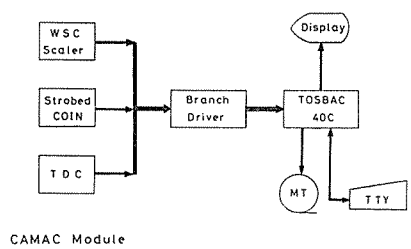

Fig. 11. On-line data acquisition system.

The contents of the CAMAC data were as follows;

(1) bit pattern of tagging counters, triggering counters, and charged particle counters (Strobed Coincidence),
(2) time difference between TAG and T (TDC),
(3) time of flight between TF and TB (TDC),
(4) clock data corresponding to spark position of wire spark chambers (Interval Scaler).

Data for one event were stored in 254 bytes.

The data are transferred to the computer event by event, and the stored data were damped onto a magnetic tape every ten events. The spark positions of wire spark chambers were monitored event by event on the display unit of the computer. Histograms of the accumulated number of events in various counters and the spectrum of TDC were displayed also.

IV. Kinematical Reconstruction of Event

The following physical quantities and information were calculated for each event;

(1) energy of the incident photon (k) which induced the reaction,

(2) emission angles (θ and ϕ) and a momentum (p) of the particle detected in the magnetic spectrometer,

(3) mass of the spectrometer particle,

(4) missing mass (M) which was calculated from k, p, and θ,

(5) whether there was any charged particle associating with the spectrometer particle or not.

IV-1. Photon Energy

The energy of a recoil electron in the bremsstrahlung process E_e' is expressed by a formula,

$$E_e' = 105 + 10(n-1) \quad \text{(MeV)}, \tag{IV-1}$$

where n is the name of the fired tagging counter ($n=1, 24$). The energy of the incident electron beam E_e is determined by the maximum magnetic field of the electron synchrotron. Since the energy transfer to target nuclei is negligibly small in the bremsstrahlung process, the energy of the tagged photon is determined as,

$$k = E_e - E_e'. \tag{IV-2}$$

In the case when only one name of the tagging counter was recorded, the energy of the tagged photon was determined by formulae (IV-1) and (IV-2). More than two names of the tagging counters were recorded in some cases. Such events came from the following two sources;

(1) geometrical overlapping between two neighbouring tagging counters,

(2) accidental coincidence between two or more different tagging counters.

The events of case (1) were measured to be 4.1% of total events. The photon energy was determined by taking the mean value of the energies corresponding to the two neighbouring counters in this case. On the other hand, the accidental events, in the case (2), were abondoned. The ratios of accidental events to the total ones depended on the intensity of the tagged photon beam, and the ratios were measured to be 2.8% and 5.8% for positive and negative polarity run of the spectrometer, respectively.

IV-2. Reconstruction of Trajectory

In order to determine the momentum of the observed particle, the reconstruction of the particle trajectory in the spectrometer was performed as follows.

(1) *Coordinates of a spark position*

As is shown schematically in Fig. 12, a combination of a horizontal clock count (n_x) and a vertical one (n_y) from the read out system of a wire spark chamber gives a spark position. The clock count represents a distance between the fiducial wire and a sparked wire. The count between two fiducial wires at both ends of the chambers N is used as a calibration of the signal velocity in the magnetostrictive line.

Using the known distances between the two ficucial wires, L_x and L_y, which were measured before and after the experiment in the accuracy of less than 1 mm, the

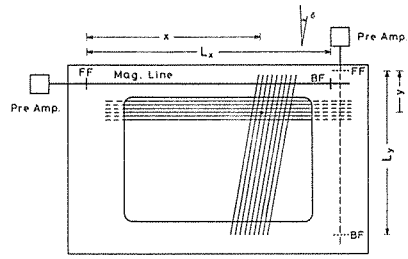

Fig. 12. Schematic view of a wire spark chamber. Coordinates of a spark point are represented by x and y.

coordinates of a spark position, (x, y), are expressed as follows;

$$y = \frac{n_y}{N_y} \cdot L_y, \quad x = \frac{n_x}{N_x} \cdot L_x + y \tan \delta, \tag{IV-3}$$

where δ represents an angle between the direction of y-wires and the direction perpendicular to x-wires, and was 0°, 10°, and $-10°$.

Since the three chambers before the magnet were set close to the target, the multiple firing events amounted to $5 \sim 15\%$ of total events. In this case, all combinations of x and y in each chamber were stored as candidates of the true spark position for further analysis.

The alignment of the whole chamber system was examined by a run without magnetic field. By measuring the deviations of spark positions from a straight line, it was found that all chambers were aligned in the accuracy with ± 1.5 mm in x and ± 0.6 mm in y.

(2) *Reconstruction of trajectory*

Because of the characteristics of the spark chamber, spark positions were not recorded on some chambers, and some chambers recorded sparks due to the background particles or spurious discharge. Reconstruction of the particle trajectory for each event was performed in the following way.

(a) When all of three chambers in front of the magnet were fired, candidates of trajectories were reconstructed by a least squares fit. In the case where multisparks were recorded, trajectories were reconstructed for all combinations of the spark positions for each chamber. Geometrical tests taking account of the sizes of the triggering counter (TF), the magnet entrance, and the target were, then, applied to the fitted candidates of trajectories. Among the candidates of trajectories passed this test, the trajectory which gave the minimum standard deviation in the fitting was selected. When this deviation was greater than 2 mm, all combinations of the spark positions in any two chambers were examined to construct trajectory following the procedure of (c).

(b) When four or three chambers were fired in the chambers downstream from the magnet, the trajectory was reconstructed in the same way as (a). A geometrical test which takes account of the sizes of the triggering counters (TM and TB) and the magnet exit were also made. The standard deviation of the accepted trajectory was less than 2 mm also.

(c) When two chambers in one side of the magnet were fired and the trajectory

of other side was accepted as described in (a) and (b), the following technique was used. Any possible straight lines were drawn between all combinations of the two spark positions in each chamber, and were considered as candidates of trajectories. The geometrical tests described in (a) and (b) were made on these candidates. Then a matching test on the candidates of trajectories which passed the geometrical tests were performed as follows. Two distances R_1 and R_2 were calculated from the obtained two trajectories l_i and l_o as seen in Fig. 13. If both of l_i and l_o represent the real trajectory, R_1 should be equal to R_2. As a measure of the difference between R_1 and R_2, we calculated a parameter d defined as,

$$d = \frac{2(R_1 \sim R_2)}{R_1 + R_2} . \qquad \text{(IV-4)}$$

Among all combinations of l_i and l_o, the one in which d was less than 0.1 was accepted.

(d) When any two chambers of each sides of the magnet were fired, the geometrical tests and the matching test were applied for all combinations of spark positions in each chamber.

By the above procedure 89% of total events were accepted as true events.

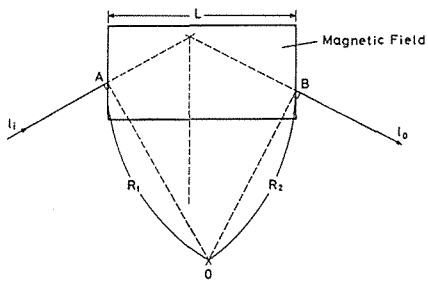

Fig. 13. Schematic drawing of the matching test of the trajectory in the spectrometer.

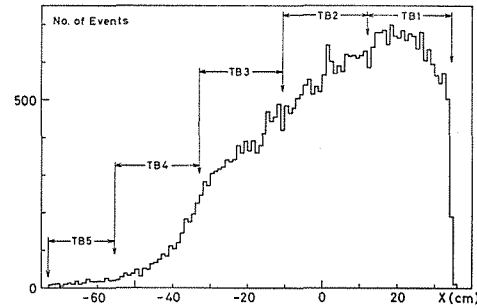

Fig. 14. Distribution of the reconstructed trajectories at TB.

Fig. 14 shows the horizontal distribution of the accepted trajectory at TB. A sharp cut due to the edge of a counter, and dips corresponding to the gaps of neighbouring counters are clearly seen in the distribution at the right positions.

The vertical distributions at the target are also shown in Figs. 15, which correspond to the reaction point distribution. Two peaks in the empty target data correspond to the upstream and downstream ends of the target container made of Mylar film.

Emission angles of the detected particles were also calculated from the trajectories. The distribution in θ and ϕ of negatively charged pions for a target full run are shown in Figs. 16.

(3) *Angular resolution*

Spatial resolutions of the chamber were estimated with the trajectories with three chambers, and were ± 0.4 mm and ± 0.5 mm for horizontal and vertical directions, respectively. Typical distributions are shown in Figs. 17. From this spatial resolu-

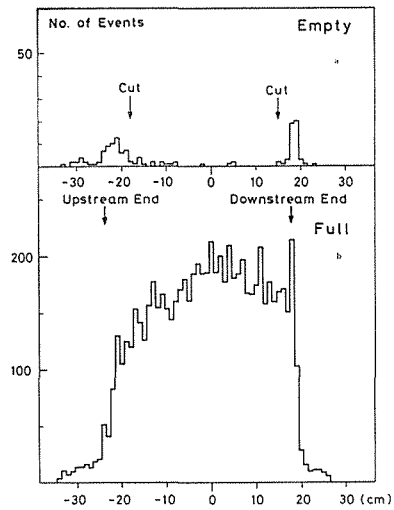

Figs. 15. Distributions of the reconstructed reaction points of (a) empty target run and (b) full target run for negative polarity run of the spectrometer.

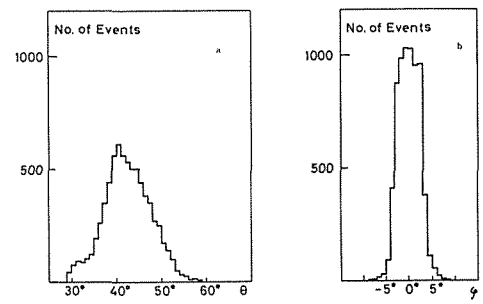

Figs. 16. Angular dependences of negative pions yield in (a) θ and (b) ϕ.

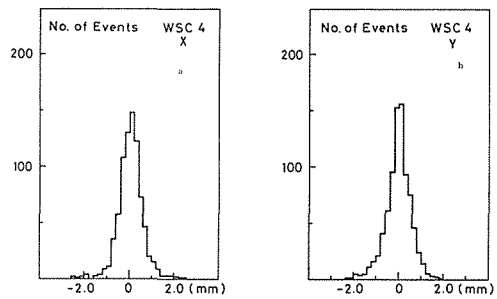

Figs. 17. Spatial resolutions of a wire spark chamber in (a) horizontal and (b) vertical.

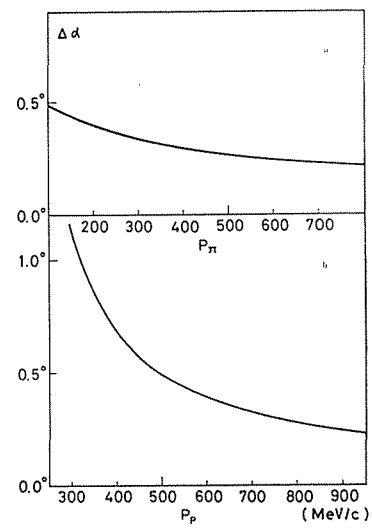

Figs. 18. Angular resolutions of the upstream wire spark chamber system for (a) pions and (b) protons.

tion, the angular resolution of the spectrometer was estimated to be less than $\pm 0.2°$. However, the multiple Coulomb scattering in the materials must take into account for the resolution, especially for low momentum protons. A Monte Carlo calculation described in Appendix B was performed to obtain the final angular resolution. The results are shown in Figs. 18 for pions and protons as a function of the momentum.

IV-3. Momentum

Since the spectrometer had angular acceptance of $\pm 5°$ in ϕ direction, we determined the momentum by projecting the trajectories of both side of the magnet on the horizontal plane. An effective edge approximation of the magnetic field was employed as shown in Fig. 19. l_i and l_o crossed the effective edges of the magnetic field at A and B, respectively. The point O is the intersection of the line at right angle to l_i at A and the line at right angle to l_o at B. $R(=\overline{OA}=\overline{OB})$ is a radius of curvature of the trajectory in the magnetic field. Since the injection angle α, the ejection angle β, and the effective length of the magnetic field L are known, the radius R can be determined by the following formula;

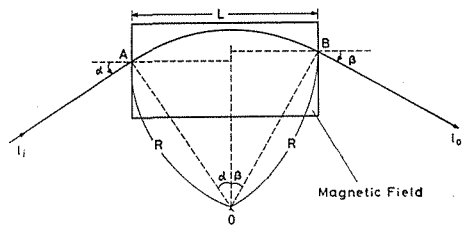

Fig. 19. A schematic drawing of the momentum reconstruction procedure.

$$R = \frac{L}{\sin\alpha + \sin\beta} \text{ (cm)}. \qquad \text{(IV-5)}$$

The momentum of the particle was calculated from R and the strength of the magnetic field H (kG),

$$p = 0.3RH \text{ (MeV/c)}. \qquad \text{(IV-6)}$$

A trajectory with a negative deflection angle, $\alpha+\beta<0$, was not accepted. The effect of the vertical component of the momentum was less than 0.4% and was corrected.

Particles lost their momenta due to the ionization in the hydrogen target and the other materials in the spectrometer, which are listed in Table 4. The momentum loss was estimated by the formula given by Livingston and Bethe with a small correction due to the density effect of atoms.[23] As the momentum loss depends on the momentum, the injection angle to the matter, and the mass of particle, the correction was made event by event. The corrections for pions and protons are shown in

Table 4. List of materials in the spectrometer.

Element	Material	Size	Thickness (g/cm²)	
Target	Liq. H_2	60 mmϕ	0.33	(θLab.=40°)
Appendix	Mylar	5 mil.	0.018	
Vacuum Jacket	Mylar	7 mil.	0.025	
TF	Scinti.	2 mm	0.21	
TM	:	3 mm	0.31	
TB	:	6 mm	0.62	
WSC Wire	Stainless Steel	100 μmϕ in 1 mm step	0.05	(for each)
Window	Mylar		0.05	(for each)
Air		~200 cm	0.24	
He		~100 cm	0.02	

Figs. 20 as a function of the momentum at a laboratory angle of 40°.

The momentum resolution $\Delta p/p$ was calculated from the following formula;

$$\Delta p/p=\sqrt{(\Delta R/R)^2+(\Delta H/H)^2}, \tag{IV-7}$$

$$\Delta R/R=\sqrt{(A\Delta L)^2+(B\Delta\alpha)^2+(C\Delta\beta)^2}, \tag{IV-8}$$

with

$$A=1/L,$$
$$B=-R\cos\alpha/L, \tag{IV-9}$$
$$C=-R\cos\beta/L.$$

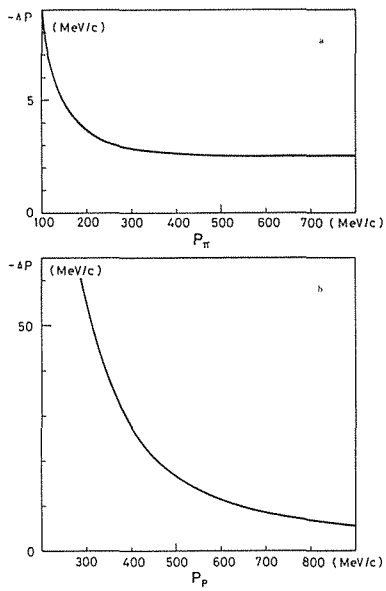

Figs. 20. Calculated momentum losses in the hydrogen target and the spectrometer for (a) pions and (b) protons.

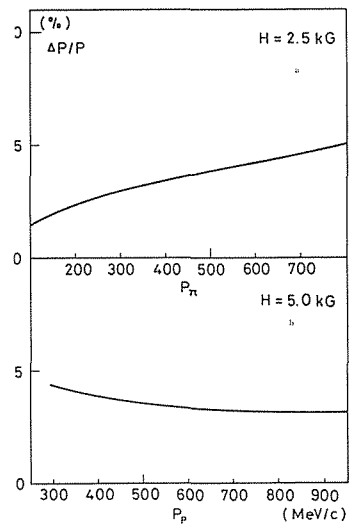

Figs. 21. Calculated momentum resolutions of the spectrometer for (a) pions at $H=2.5$ kG and (b) protons at $H=5.0$ kG.

These formulae show that momentum resolution depends on the variation of the magnetic field $\Delta H/H$, the error on the effective length of the magnetic field ΔL, and the error in the injection angle $\Delta\alpha$, and the error in the ejection angle $\Delta\beta$.

The strength of the magnetic field had been monitored by reading the current of the magnet during the experiment, and $\Delta H/H$ were less than $\pm 0.5\%$ and $\pm 0.3\%$ for $H=2.5$ kG and $H=5.0$ kG run, respectively. $\Delta L/L$ was estimated to be less than $\pm 0.3\%$ as described in section III–3. The resultant resolutions are shown in Figs. 21.

IV-4. Identification of Particle

Since the present experiment has been performed at the energies lower than the kaon threshold, particle which can pass through the spectrometer are electrons (positrons), muons, pions, and protons.

TOF (t) between TF and TB was measured to discriminate protons from the other particles. The path length (l) between the two counters was calculated from the trajectory. Then the velocity of the observed particle was expressed as,

$$c\beta = \frac{l}{t}, \qquad \text{(IV-10)}$$

where c is the light velocity. Two dimensional plots of p and β was useful for the identification of the particle as seen in Fig. 22. In these plots, the identification of protons were made at the cut off velocities which correspond to the velocities of particles having mass of 600 MeV. The time resolution of TOF was estimated to be ± 1.0 nsec.

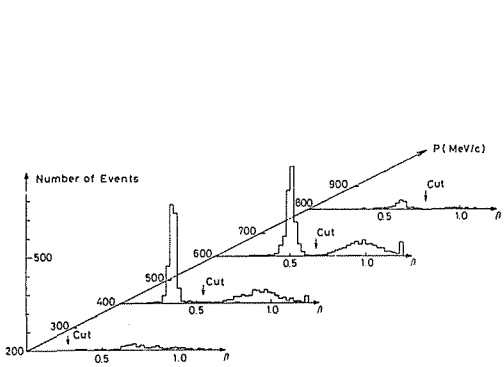

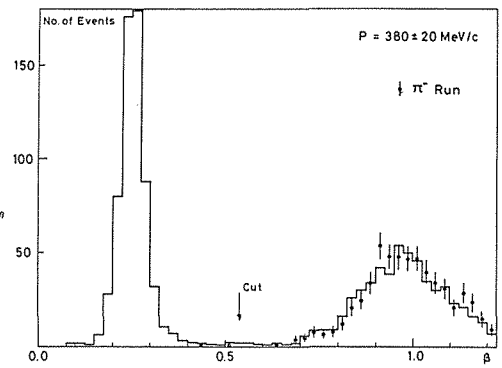

Fig. 22. Distributions of the calculated betas obtained from the time of flight of the spectrometer particles in a positive polarity run. The histogram show the distribution at some typical momenta with 40 MeV/c width.

Fig. 23. Comparison of the β-distribution in positive and negative polarity runs. The solid line represents the β-distribution in a positive polarity run at the momentum of 380 MeV/c, and the closed circles represent the distribution in a negative polarity run at the same momentum. Total numbers of the lighter particles are normalized between the two distribution.

The probability of misidentification of protons from the other particles was negligibly small even in the higher momentum. As shown in Fig. 23, this fact was demonstrated by comparing positive polarity run to negative polarity run. Although the random events due to the accidental coincidence between the three triggering counters were seen in the spectrum, accidental events were 3% and 0.7% of the total events for negative polarity run and positive polarity run, respectively.

The particles having the higher velocities than the cut off velocities were accepted as the pions. Since muons are expected to come from the pion decay, the muons could not be discriminated from pions. A description of the decay correction for pions will be given in Chapter V.

The discrimination of electrons and positrons from pions were also not made in this experiment. The electrons and positrons background in the pions will be described in section V–6.

IV-5. Missing Mass

The missing mass associated with the spectrometer particle is calculated from the measured quantities by the relation,

$$M^2=(k+m_p-E)^2-P^2, \tag{IV-11}$$

with

$$P^2=k^2+p^2-2kp\cos\theta,$$
$$E=\sqrt{p^2+m^2},$$

where M, m_p, and m represent the missing mass, proton mass, and the spectrometer particle mass, respectively.

The resolution of the missing mass is calculated by the following formulae,

$$\frac{\Delta M}{M}=\frac{1}{M}\sqrt{\left(A\frac{\Delta p}{p}\right)^2+(B\Delta\theta)^2+(C\Delta k)^2}, \tag{IV-12}$$

where

$$A=p\frac{\partial M}{\partial p}=\frac{1}{M}\left\{k\cos\theta-(k+m_p)\frac{p}{E}\right\},$$
$$B-\frac{\partial M}{\partial\theta}=-\frac{kp\cos\theta}{M}, \tag{IV-13}$$
$$C=\frac{\partial M}{\partial k}=\frac{m_p-E+p\cos\theta}{M}.$$

It is worth noticing that the resolution is inverse proportional to the missing mass squared.

The missing mass resolution were shown in Figs. 24 for pions and protons.

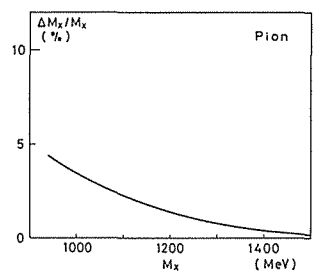

Fig. 24-a

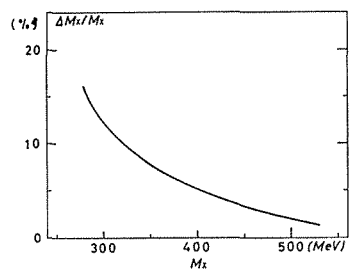

Fig. 24-b

Figs. 24. Calculated resolutions of the missing mass for (a) pions and (b) protons.

IV-6. Identification of the Reaction

It is necessary to detect any one of charged particle accompanied with the spectrometer particle for reaction identification. The charged particle hodoscopes were used for this purpose.

The separation between single and double pion photoproduction could be easily made by calculating missing mass associated with the spectrometer particles. For double pion production process, the type of reactions were identified by use of the hodoscopes information.

The detection efficiency by the charged particle hodoscopes were calculated for double pion photoproduction process by a Monte Carlo method. The efficiency was relatively high and almost independent of the reaction mechanism as shown in

Figs. 25, for example. This was due to the large solid angle of the hodoscopes. The efficiency was measured in the negative pion run, where exists only one final state $\pi^-\pi^+p$, and the hodoscopes detected π^+ and/or p accompanied with the spectrometer particle of π^-. As shown in Fig. 26, the agreement between the measured efficiencies

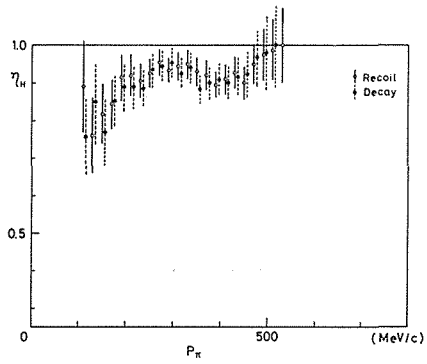

Fig. 25-a

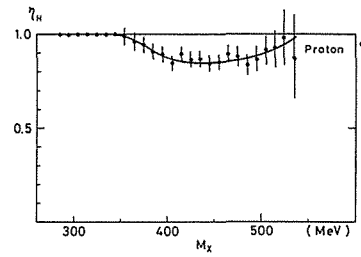

Fig. 25-b

Figs. 25. (a) Detection efficiency of the charged particle hodoscope. Detection efficiencies for the case when the spectrometer particles are pions. Open circles and closed circles correspond to the case when the spectrometer particle were recoil pions and decay pions, respectively. (b) Detection efficiency for the case when the spectrometer particles were protons. The Monte Carlo calculation was performed for the quasi-two body reaction of $\gamma p \to \pi \Delta$.

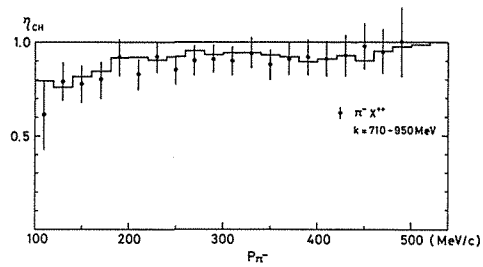

Fig. 26. Detection efficiency of the charged particle hodoscopes for negative pions measured in the negative polarity run. Closed circles represent the experimental results. The solid line represents the results of the Monte Carlo calculation.

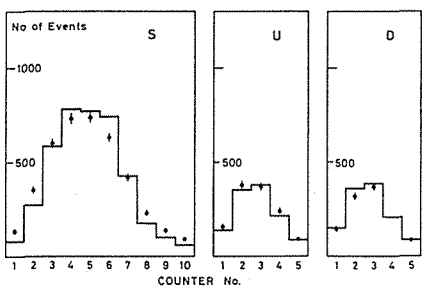

Fig. 27-a

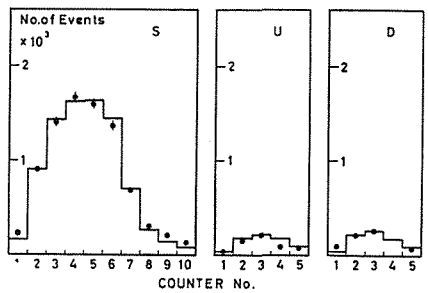

Fig. 27-b

Fig. 27. Yield distribution of the charged particle hodoscopes. The solid line represents the results of the Monte Carlo calculations and was normalized to that of the experimental one. (a) The spectrometer particles were pions and (b) the spectrometer particles were protons.

and the calculated ones are good. The distributions of events in the hodoscope are also in good agreement with the Monte Carlo calculation as shown in Figs. 27.

The accidental coincidence rates between the signal from hodoscopes (CH) and the master signal were estimated by TOF spectrum between the two signals, and were 3% and 1% of total events for the positive polarity run and negative polarity run, respectively. The TOF spectrum for the proton run is shown in Fig. 28.

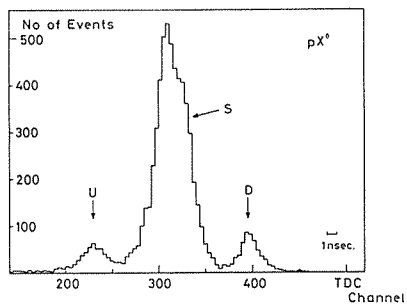

Fig. 28. TOF spectrum between T and CH. The signals from S and D were delayed by 10 nsec and 20 nsec to U, respectively, in order to separate them each other.

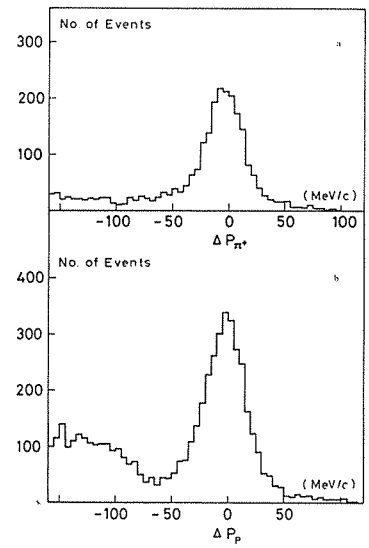

Figs. 29. Distributions of the differences between the measured momenta and the calculated ones from k and θ assuming two-body kinematics for the reactions (a) $\gamma p \rightarrow \pi^+$ and (b) $\gamma p \rightarrow \pi^\circ p$.

IV-7. Selection of Event

The background coming from the Mylar windows of the target container were seen in the distribution of the empty target run shown in Fig. 15. The events fall inside the cut off positions in Fig. 15 were selected.

Although the spectrometer accepted the particles with laboratory angles between 30° and 60°, only the particles of emission angle smaller than 51° and larger than 37° were selected.

After these selections were made, 11.2 k reconstructed events for protons, 14.9 k for positive pions, and 7.4 k for negative pions were remained for further analyses.

IV-8. Accuracy of the Reconstruction

In the present experiment pions and protons from single pion photoproduction $\gamma p \rightarrow \pi^+ n$ at a center of mass angle $\theta_\pi^* \sim 60°$ and $\gamma p \rightarrow \pi^\circ p$ at $\theta_\pi^* \sim 90°$ were measured simultaneously as stated in section IV–6. By selecting these events, an internal consistency between the reconstructed k, p, and θ was examined. Since masses of all particles are known, number of unknown variables in this experiment are two. Anyone of the three variables k, p, and θ can be, therefore, calculated from the rest of two variables. Figs. 29 show the distribution of the difference between the re-

constructed momentum p and the calculated momentum from k and θ for $\gamma p \to \pi^+ n$ and $\gamma p \to \pi^\circ p$. The results are in good agreements each other, so that the reconstruction of the three variables were proved to be performed correctly.

V. Data Reduction

V-1. Laboratory Cross Section Formula

Double differential cross sections with respect to momentum in the laboratory system are given by the following formula for pions and protons;

$$\frac{d^2\sigma}{d\Omega dp} = \frac{Y}{N_\gamma \cdot N_T \cdot l_0 \cdot \Delta p \cdot \Delta\Omega}, \qquad \text{(V-1)}$$

where

N_γ ; number of the incident photons,
N_T ; number of the target protons per unit volume,
l_0 ; length of the liquid hydrogen target,
Δp ; bin width of momentum,
$\Delta\Omega$; solid angle of the spectrometer, which is a function of momentum,
Y ; yield of pions or protons in the momentum range from $p-\Delta p/2$ to $p+\Delta p/2$.

For cross sections with respect to the missing mass, formula (V-1) is modified using the variable M, missing mass;

$$\frac{d^2\sigma}{d\Omega_M dM} = \frac{Y_M}{N_\gamma \cdot N_T \cdot l_0 \cdot \Delta M \cdot \Delta\Omega_M}, \qquad \text{(V-2)}$$

where

ΔM ; bin width of the missing mass,
$\Delta\Omega_M$; solid angle of the spectrometer, which is a function of the missing mass,
Y_M ; yield of pions or protons in the missing mass range from $M-\Delta M/2$ to $M+\Delta M/2$.

The following sections describe the details of the method to determine N_γ, the culculation of $\Delta\Omega$, and the corrections for yield.

V-2. Number of Photons

The added counts of adjacent four tagging counters, corresponding to 40 MeV photon energy bin, were monitored by scalers. The number of the tagged photons was obtained from the scaler data after a few corrections.

As mentioned in section III-1, a part of the tagged electrons was not accompanied with photon of the proper energy. The factors η_i were multiplied for each scaler data to correct the tagged photon flux. The attenuation of the incident photons in the hydrogen target was calculated to be 2% using the data of total absorption cross section of photons.[24] After these corrections were made, the number of the tagged photons was compared with the number of photons which was estimated from the thick-walled ionization chamber. Both of them agreed well within an accuracy of $\pm 1.5\%$.

Moreover, the correction due to the multi-tagging events as stated in section IV-1 were also made. The corrections were 2.8% and 5.8% for positive polarity run

and negative polarity run, respectively.

V-3. Acceptance of the Spectrometer

A trajectory of a particle in the spectrometer can be expressed in terms of the reaction point $\boldsymbol{r}$, the emission angles θ and ϕ, and the momentum p. The acceptance of the spectrometer, which is a function of the momentum, can also be expressed by the formula:

$$\Delta\Omega(p)=\frac{\Omega_0}{N_0}\cdot\int_{p_{\min}}^{p_{\max}}\int_{\phi_{\min}}^{\phi_{\max}}\int_{\cos\theta_{\min}}^{\cos\theta_{\max}}\int_{\boldsymbol{R}}\varepsilon(\boldsymbol{r},\theta,\phi,p)\mathrm{d}^3\boldsymbol{r}\mathrm{d}\cos\theta\mathrm{d}\phi\mathrm{d}p, \tag{V-3}$$

where

$$\Omega_0=(\phi_{\max}-\phi_{\min})(\cos\theta_{\max}-\cos\theta_{\min}),$$

$$N_0=\Omega_0\cdot\Delta p\cdot\int_{\boldsymbol{R}}\mathrm{d}^3\boldsymbol{r}.$$

$p_{\max}$, $p_{\min}$, $\phi_{\max}$, $\phi_{\min}$, $\cos\theta_{\max}$, and $\cos\theta_{\min}$ were the limits of the area of integration about p, ϕ, and θ, respectively. $\boldsymbol{R}$ was the area of integration of the reaction point. The integrand is a function defined as,

$\varepsilon(\boldsymbol{r},\theta,\phi,p)=1$; trajectory is inside the spectrometer,

0; trajectory is outside the spectrometer.

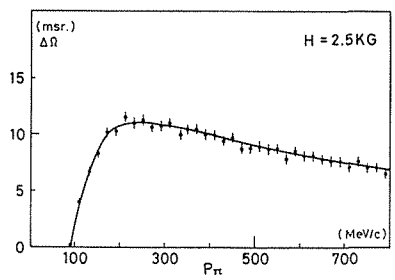

Fig. 30-a

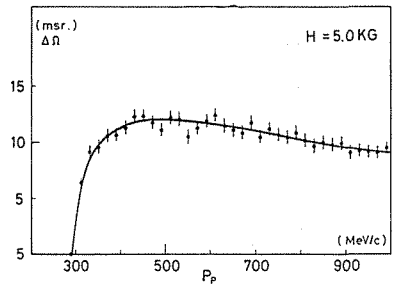

Fig. 30-b

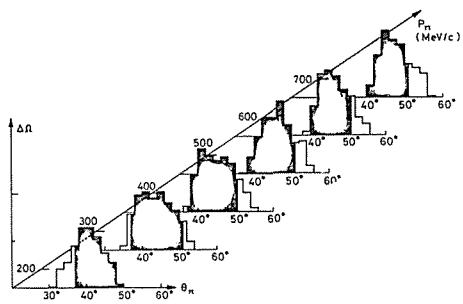

Fig. 30-c

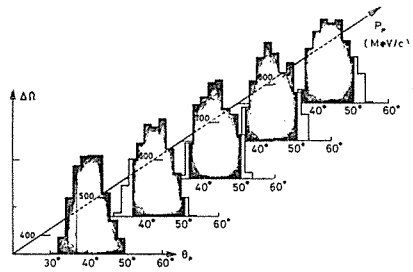

Fig. 30-d

Figs. 30. Acceptances of the spectrometer were calculated by a Monte Carlo program for (a) pions and (b) protons. Angular acceptances of the spectrometer are shown for (c) pions and (d) protons.

The acceptance given by formula (V–3) was calculated by a Monte Carlo method. The effects of the multiple Coulomb scattering and the momentum loss in the materials along the trajectories were considered in the calculation. For pions, $\pi \to \mu\nu$ decay was also considered, and the details of these effects were discussed in the following section.

The procedure of the Monte Carlo calculation is given in Appendix B. The calculated acceptance are shown in Fig. 30–a and 30–b. The angular acceptances are shown in Fig. 30–c and 30–d.

V-4. Sizes of Corrections

The loss of yield due to the multiple Coulomb scattering in single momentum bin was $2 \sim 3\%$ for both of pions and protons, but approximately the same amount of yields came into the bin from other momentum bins. Finally no correction was made for this effect.

Existing data of elastic and inelastic cross sections of pion-nuclei and proton nuclei interactions were used for the calculation of the nuclear absorption correction. The resulting corrections are shown in Fig. 31.

The pion decay is given by the formula;

$$f_{\text{decay}} = 1 - \exp(-\mu l / c^2 \tau_0 p), \qquad \text{(V–4)}$$

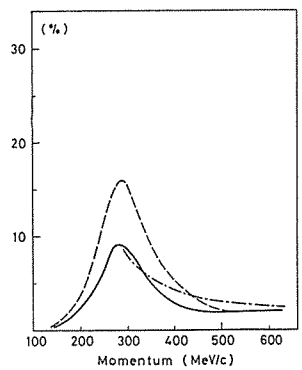

Fig. 31. The nuclear absorption in the hydrogen target and the spectrometer. Solid curve, dashed one, and dash-dotted one correspond to negative pions, positive pions, and protons, respectively.

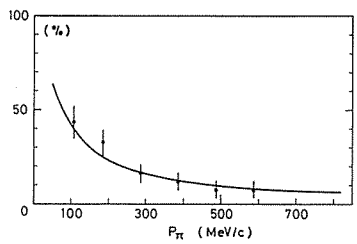

Fig. 32. Calculated rate of decayed pions in the spectrometer (closed circles). The solid curve represents formula (V–4) evaluated at $l = 300$ cm.

where μ is the pion mass, l is the path length of a pion from the target to TB, and τ_0 is the life time of a pion at rest. Since muons produced in the spectrometer were not distinguished from pions in the experiment, f_{decay} is not directly applicable for the decay correction. The decayed muons are treated as pions in the trajectory reconstruction, Monte Carlo calculations were performed in order to estimate the rate in which decayed muons passed the reconstruction criteria. The most of the decayed muons did not pass the reconstruction criteria, because of rather severe criteria for the trajectories. Therefore, formula (V–4) turned out to be applicable. Results are shown in Fig. 32.

V-5. Subtraction of Accidental Coincidence Yield

Accidental coincidence events between TAG and T was subtracted from the yield. The rate of accidental coincidence events to the total ones is proportional to the intensity of the tagged photon beam.

There were two types of accidental coincidences between TAG and T:

(a) accidental coincidence between T signal induced by a non-tagged photon and a tagging signal,

(b) accidental coincidence between T signal induced by a tagged photon and the other tagging signal.

In order to know the shape of the momentum spectra due to the accidental

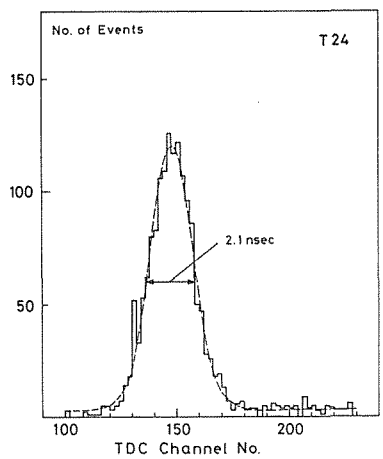

Fig. 33-a

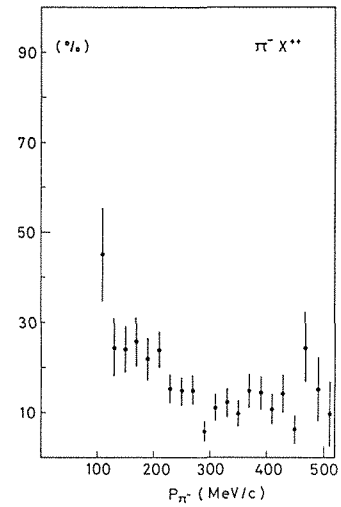

Fig. 33-b

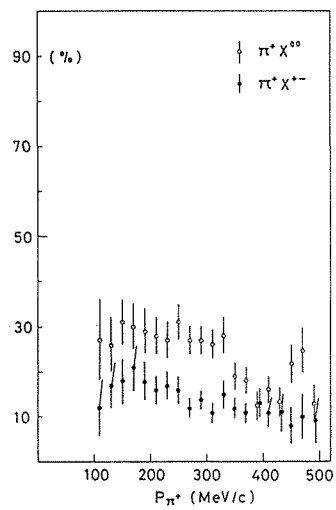

Fig. 33-c

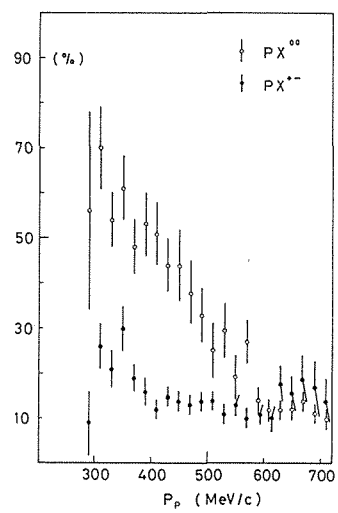

Fig. 33-d

Figs. 33. (a) TOF spectrum between T and T_{24}. Ratios of the accidental coincidence events to the total events for (b) negative pions, positive pions, and (d) protons.

coincidence events of types (a) and (b), the momentum spectrum of the off-timing events, which were known from the TOF spectrum as shown in Fig. 33–a, were analyzed. In this case the normalization of the spectrum was determined by measuring the rate of the delayed coincidence between TAG and T. Figs. 33–b, 33–c, and 33–d show these spectra for negative pions, positive pions, and protons, respectively. A large peak below 500 MeV/c for protons, especially for $pX^{\circ\circ}$ spectrum, was interpreted as the first resonance excitation in the reaction $\gamma p \to \pi^{\circ} p$ induced by non-tagged photons. Bumps below 200 MeV/c for pions might be due to an electron (positron) background by low energy non-tagged photons. The rates of the reconstructed accidental events to the total ones amounted to 13.8% for protons, 16.1% for positive pions, and 17.8% for negative pions.

These accidental coincidence yields were subtracted from the total yields in each momentum and missing mass bin.

V-6. Subtraction of Empty Target Yield

Empty target yields were 6.5% and 8.9% of the full target yields for the positive polarity run and the negative polarity run, respectively. Most of the empty target yield came from two Mylar windows of the target container as shown in Figs. 15. Since this kind of the empty target yield were eliminated by the selection of events by setting the cuts in the distribution of the reaction points as described in section IV–7, the ratio of the empty target yields to the full target ones was reduced to 1.0%. The ratio was consistent with the value estimated from remaining gas in the empty target. These yields were subtracted from the total yield.

V-7. Electron Background

Since electrons (positrons) were not discriminated from pions in this experiment, it was needed to subtract the electron background from the total yield for pions.

In an ordinary experiment using the bremsstrahlung photon beam, the copious background of low momentum electrons coming from the pure electro-magnetic processes like pair production and compton scattering is a serious problem. But in this experiment, electrons produced by non-tagged photons which has energy lower than 710 MeV and higher than 950 MeV were detected only as the accidental coincidence between TAG and T. Therefore, this kind of electrons were subtracted from the total yield as described in section V–5.

The electrons originated in the Mylar windows of the target container were not accepted as events by the cuts in the reaction points.

The electrons induced by tagged photons from the hydrogen target were estimated by integrating the Hough formula,[25] and the results showed that the ratios of electron background to the pion yield were less than 3% at about 100 MeV/c and less than 1% above 150 MeV/c as shown in Fig. 34. As the ratio was negligibly small, no correction was made for this kind of electron background.

V-8. Errors

There were a number of sources of systematic errors for the absolute values of the cross sections. These were as follows.

(a) Uncertainty in the number of the tagged photons due to the accuracy in efficiency and the accidental coincidence subtraction.

(b) Uncertainty in the number of target protons due to the accuracy in esti-

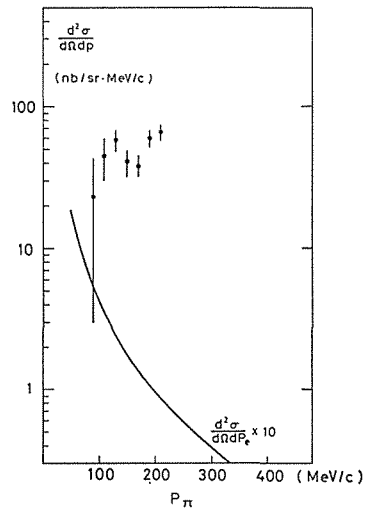

Fig. 34. Double differential cross sections of negative pions at $k=730$ MeV (closed circles). The solid curve represents the calculated cross sections by Hough formula for electron positron pair production from hydrogen at a laboratory angle of 37°.

mating the contraction of the target container at low temperature, and the density of liquid hydrogen.

(c) Uncertainty in the acceptance of the spectrometer due to the accuracy of the Monte Carlo calculation and of the measurements of the positions of the elements in the spectrometer.

(d) Uncertainty in corrections for yield due to the accuracy in estimating empty target yield, contribution of electron (positron) background, identification of pions and protons, reconstruction efficiency of the events, yield losses, and accidental coincidence yield.

(e) Uncertainty in the detection efficiency of the charged particle hodoscopes due to the accuracy of the Monte Carlo calculation described in section IV–6.

The evaluated values are listed in Table 5.

Table 5. Systematic errors (Half Width in %).

		π^-X^{++}	π^+X°	π^+X^{+-}	$\pi^+X^{\circ\circ}$	pX°	pX^{+-}	$pX^{\circ\circ}$
a)	Number of Photons				2			
b)	Number of Target Protons				1			
c)	Solid Angle				5			
d)	Yield	8∼5	9∼5	7∼5	9∼5	10∼5	8∼4	45∼4
e)	Charged Particle Detection Efficiency	0	0	6	10∼15	0	6	10∼70
	Quadratic Sum	10∼7	11∼7	11∼10	15∼17	11∼7	11∼9	46∼70

VI. RESULTS AND DISCUSSION

VI-1. Results

The momentum and missing mass spectra of reactions (II–1),..., (II–7) measured at the angular range between 37° and 51° in the laboratory system are shown in Figs.

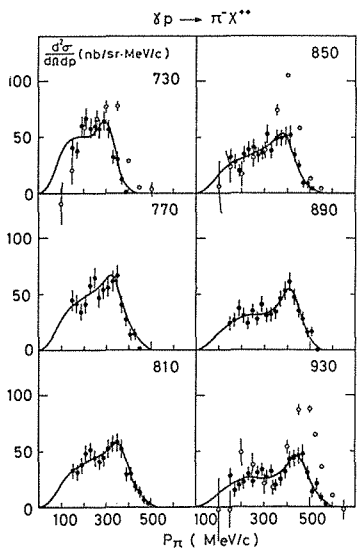

Fig. 35-a

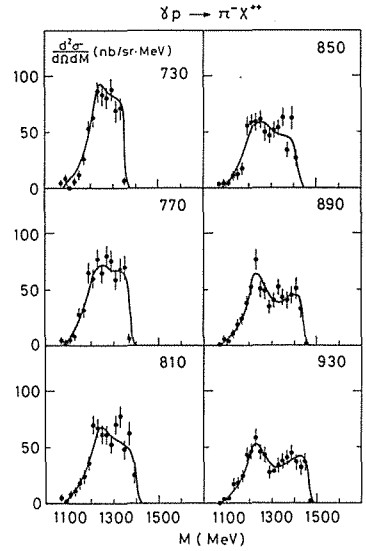

Fig. 35-b

Figs. 35. (a) Momentum spectra and (b) missing mass spectra of $\gamma p \to \pi^- X^{++}$. Closed and open circles represent the present results and the results by Fukui *et al.*[8], respectively.

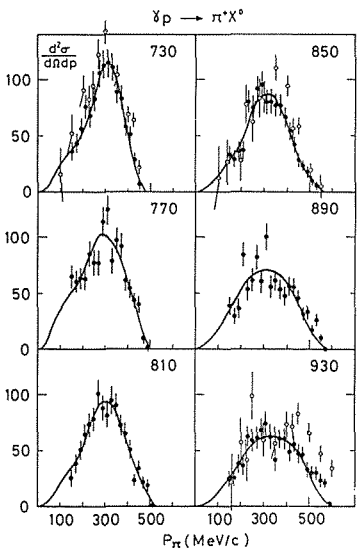

Fig. 36-a

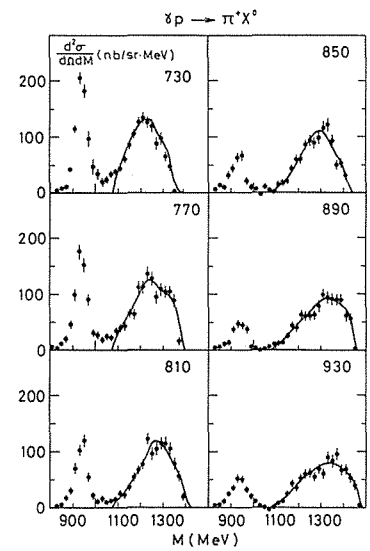

Fig. 36-b

Figs. 36. (a) Momentum spectra and (b) missing mass spectra of $\gamma p \to \pi^+ X^\circ$. Closed and open circles represent the present results and the results by Fukui et al.[8], respectively.

35～41 together with the results by Fukui *et al.*,[8] and numerical values of the double differential cross sections of these reactions are listed in Tables 6～9. The errors attached to the data are statistical ones for reactions (II–1), (II–2), and (II–5). But the errors attached to the spectra of reactions (II–3), (II–4), (II–6), and (II–7) include also the systematic errors in the charged particle detection efficiencies described in section V–8.

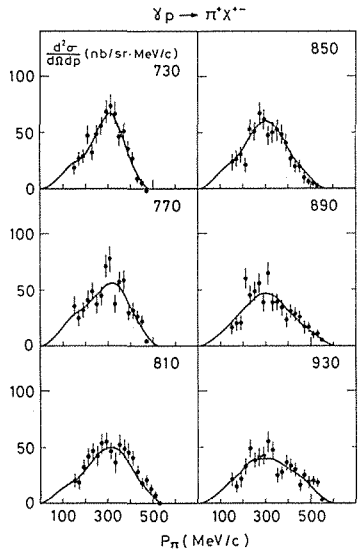

Fih. 37-a

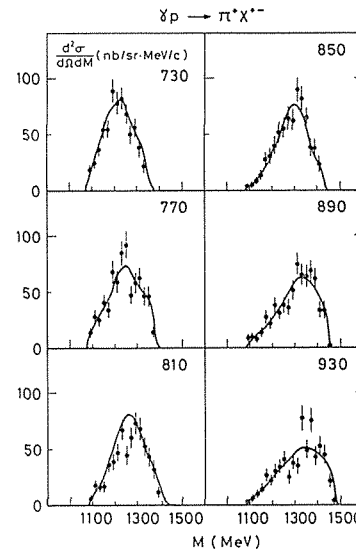

Fig.37-b

Figs. 37. (a) Momentum spectra and (b) missing mass spectra of $\gamma p \rightarrow \pi^+ X^{+-}$.

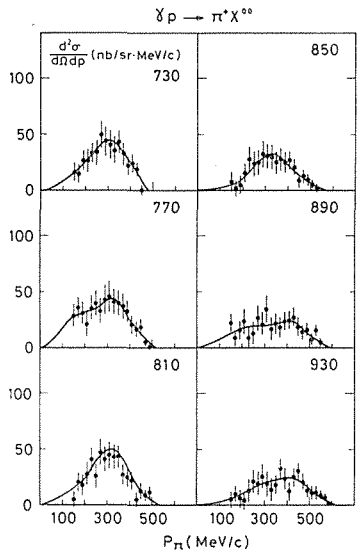

Fig. 38-a

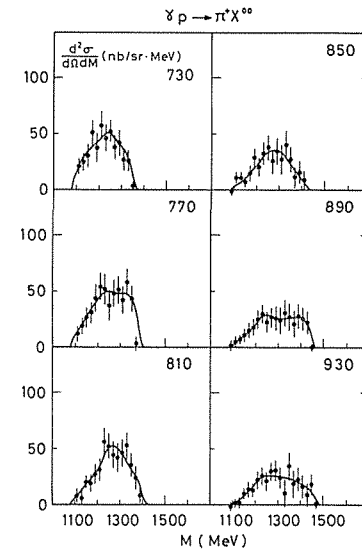

Fig. 38-b

Figs. 38. (a) Momentum spectra and (b) missing mass spectra of $\gamma p \rightarrow \pi^+ X^{00}$.

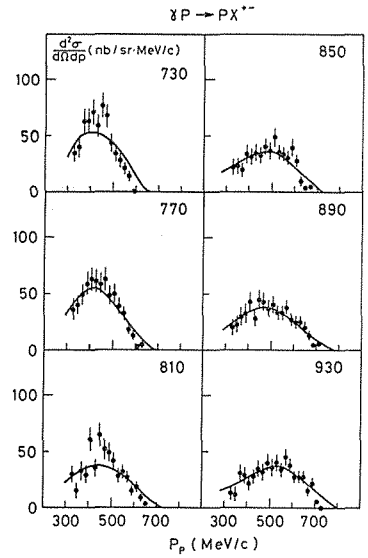

Fig. 39-a

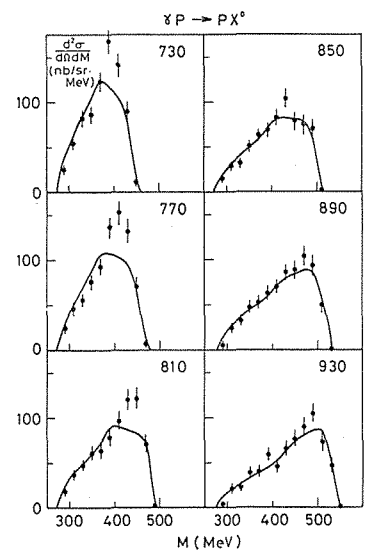

Fig. 39-b

Figs. 39. (a) Momentum spectra and (b) missing mass spectra of $\gamma p \to pX^{\circ}$.

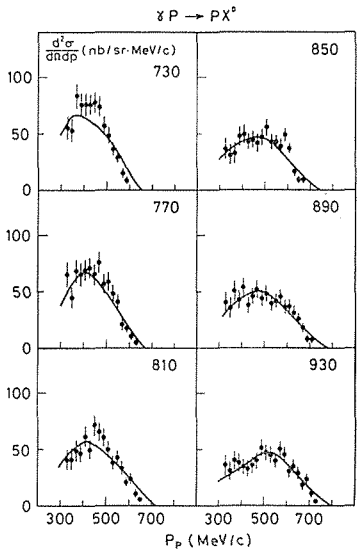

Fig. 40-a

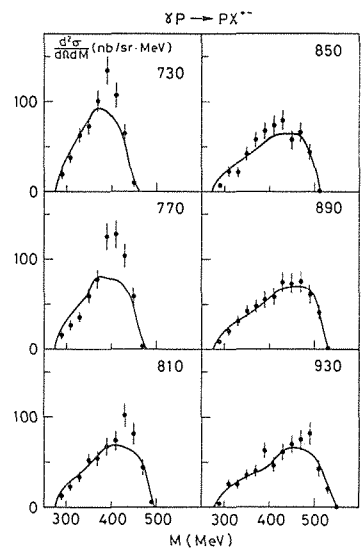

Fig. 40-b

Figs. 40. (a) Momentum spectra and (b) missing mass spectra of $\gamma p \to pX^{+-}$.

These spectra indicate the following qualitative features.

(a) In the missing mass spectra of reaction (II–2) (Fig. 36–b), the neutron peak due to the reaction $\gamma p \to \pi^+ n$ is clearly seen. However, the pions from the reaction $\gamma p \to \pi^+ n$ are eliminated in the momentum spectra (Fig. 36–a).

(b) The spectra of $\pi^- X^{++}$ (Figs. 35) show a clear peak of Δ^{++} and a broad bump in the lower momentum (higher missing mass) region coming from the decay of $\Delta^{\circ} \to \pi^- p$ in the reaction $\gamma p \to \pi^+ \Delta^{\circ}$.

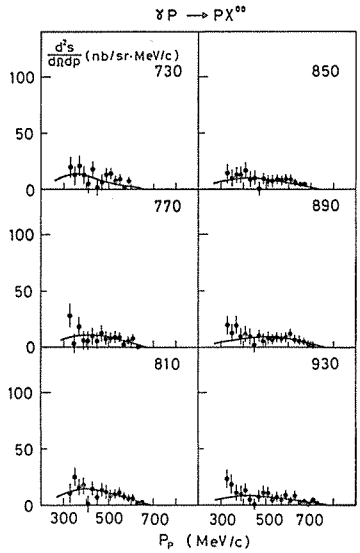

Fig. 41-a

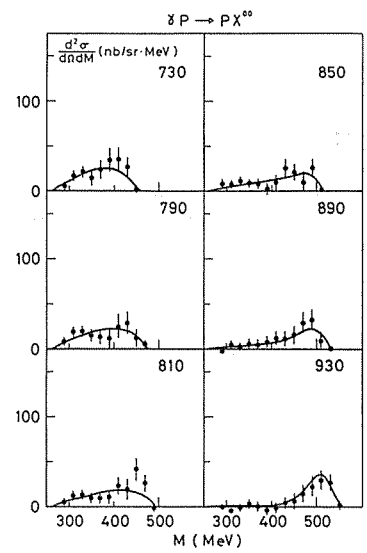

Fig. 41-b

Figs. 41. (a) Momentum spectra and (b) missing mass spectra of $\gamma p \rightarrow pX^{\circ\circ}$.

Table 6. Double differential cross sections with respect to the pion momentum in the laboratory system at $\theta_\pi = 37^\circ - 51^\circ$.

k (MeV)	p (MeV/c)	$d^2\sigma/d\Omega dp$ (nb/sr·MeV/c)			
		π^+X^{++}	π^+X°	π^+X^{+-}	$\pi^+X^{\circ\circ}$
730	150	40.8±7.6	36.0± 7.7	18.7± 5.9	17.2± 7.8
	170	38.0±7.0	42.5± 7.8	27.3± 6.5	15.3± 7.9
	190	59.8±8.3	56.1± 8.5	28.9± 6.5	27.2± 8.6
	210	66.6±8.7	75.5± 9.6	48.3± 8.1	27.2±10.0
	230	55.8±7.5	65.7± 9.1	32.0± 6.7	33.8± 9.3
	250	59.5±7.8	83.3±10.3	49.3± 8.0	34.0±10.7
	270	57.9±7.8	106.0±11.6	55.8± 8.5	50.2±11.9
	290	65.3±8.1	112.9±12.2	69.1± 9.7	43.8±12.7
	310	56.6±7.7	115.1±12.2	73.9±10.0	41.2±12.9
	330	33.0±6.0	102.8±11.6	66.8± 9.6	36.0±12.2
	350	31.2±5.7	88.5±10.0	45.7± 7.6	42.8±10.2
	370	13.1±4.2	83.8± 9.6	50.6± 8.0	33.0±10.0
	390	1.0±2.4	58.0± 8.1	36.4± 6.8	21.6± 8.3
	410		50.9± 7.4	26.8± 5.7	24.1± 7.5
	430		28.1± 5.5	9.4± 3.4	18.7± 5.5
	450		6.7± 4.2	5.9± 3.1	6.7± 4.2
770	150	45.3±8.7	64.9±10.1	36.1± 8.1	28.2±10.2
	170	42.4±7.9	60.3± 9.3	24.6± 6.6	35.7± 9.3
	190	33.9±7.0	63.5± 9.4	32.2± 7.1	31.3± 9.5
	210	41.2±7.6	62.6± 9.4	41.2± 7.9	21.4± 9.7
	230	58.1±8.3	84.7±10.6	49.1± 8.5	35.6±10.9
	250	65.4±8.8	77.2±10.6	37.1± 7.5	40.1±10.7
	270	46.8±7.6	77.1±10.7	44.6± 8.0	32.5±11.0
	290	53.7±7.9	114.0±12.9	71.0±10.3	43.0±13.4
	310	56.0±8.3	124.1±13.3	77.9±10.8	47.2±13.9
	330	62.3±8.3	78.0±10.9	37.3± 7.7	40.7±11.0

Table 6. (continued)

k (MeV)	p (MeV/c)	$d^2\sigma/d\Omega dp$ (nb/sr·MeV/c)			
		π^-X^{++}	π^+X°	π^+X^{+-}	$\pi^+X^{\circ\circ}$
	350	67.3±9.1	96.7±11.0	57.0± 8.9	39.8±11.4
	370	40.5±7.2	94.4±10.7	57.7± 9.0	36.7±11.2
	390	28.1±6.0	61.0± 8.7	28.7± 6.5	32.8± 8.8
	410	13.8±4.4	53.5± 8.0	32.2± 6.5	21.4± 8.2
	430	14.9±4.6	43.4± 7.0	26.4± 5.6	17.0± 7.2
	450	1.0±1.7	40.3± 7.2	21.8± 5.3	18.5± 7.3
	470		9.1± 4.3	4.0± 2.5	5.1± 4.3
	490		2.1± 2.7	0.9± 1.5	1.2± 2.7
810	150	32.8±7.2	25.0± 7.2	20.1± 6.3	4.9± 7.3
	170	31.0±6.6	38.3± 7.8	18.3± 5.8	20.0± 7.8
	190	38.4±7.0	49.6± 8.5	31.7± 7.0	17.9± 8.7
	210	48.3±7.8	63.7± 9.3	35.7± 7.3	28.0± 9.5
	230	50.8±7.4	72.9± 9.8	32.1± 7.0	40.8± 9.9
	250	43.9±7.0	78.2±10.4	52.8± 8.6	25.5±10.9
	270	41.4±6.9	101.4±11.7	54.2± 8.7	47.2±12.0
	290	44.1±6.9	87.6±11.3	46.3± 8.3	41.3±11.5
	310	52.7±7.7	81.4±10.9	36.4± 7.3	45.0±11.0
	330	57.4±8.1	95.2±11.6	51.8± 8.7	43.3±11.8
	350	58.3±8.0	90.1±10.5	47.4± 8.0	42.7±10.7
	370	51.7±7.7	72.3± 9.4	45.3± 7.8	27.1± 9.7
	390	30.1±5.9	65.0± 8.8	39.7± 7.4	25.3± 9.0
	410	30.7±5.9	50.4± 7.7	28.1± 6.0	22.3± 7.8
	430	19.3±4.9	23.1± 5.3	18.0± 4.6	5.1± 5.5
	450	13.8±3.9	34.3± 6.6	20.9± 5.1	13.3± 6.7
	470	7.2±3.3	21.4± 5.4	12.9± 3.8	8.5± 5.4
	490	4.0±2.4	19.4± 4.8	7.2± 2.9	12.2± 4.8
	510		−0.3± 1.8		
850	150	32.1±7.2	32.8± 7.8	24.5± 6.7	8.4± 7.9
	170	28.3±6.4	28.6± 7.1	27.1± 6.7	1.5± 7.4
	190	20.1±5.5	35.9± 7.6	31.1± 6.9	4.8± 7.9
	210	35.3±6.8	37.5± 7.8	21.3± 6.0	16.1± 7.9
	230	39.4±6.6	80.5±10.2	52.8± 8.6	27.7±10.6
	250	43.3±6.9	74.8±10.3	50.9± 8.4	23.9±10.7
	270	34.3±6.3	92.0±11.3	67.4± 9.7	24.6±11.0
	290	36.1±6.2	94.9±11.7	61.5± 9.4	33.4±12.2
	310	53.0±7.7	79.5±10.8	48.3± 8.3	31.2±11.1
	330	37.9±6.6	79.9±10.8	50.0± 8.5	29.9±11.1
	350	49.1±7.4	77.2± 9.8	52.0± 8.4	25.2±10.2
	370	49.2±7.5	76.7± 9.6	49.0± 8.1	27.7±10.0
	390	51.4±7.6	65.5± 8.8	40.9± 7.4	24.6± 9.1
	410	52.4±7.6	53.6± 7.9	26.7± 5.8	26.9± 7.9
	430	33.7±6.3	41.7± 6.8	20.5± 4.9	21.3± 6.8
	450	24.5±5.2	28.5± 6.2	19.7± 5.0	8.8± 6.3
	470	9.0±3.6	22.6± 5.5	10.0± 3.4	12.6± 5.5
	490	9.1±3.3	17.4± 4.6	7.1± 2.8	10.3± 4.5
	510	3.9±2.1	10.2± 3.6	5.1± 2.3	5.1± 3.6
	530		4.8± 2.7	3.3± 1.9	1.5± 2.7
	550		−1.0± 0.6		
890	150	23.5±6.4	38.9± 8.3	17.4± 6.0	21.5± 8.3
	170	26.8±6.3	28.8± 7.2	20.0± 6.0	8.8± 7.3
	190	36.5±6.9	36.2± 7.7	20.6± 5.9	15.6± 7.8
	210	31.4±6.6	84.4±10.4	60.0± 9.3	24.4±11.0

Table 6. (continued)

k (MeV)	p (MeV/c)	$d^2\sigma/d\Omega dp$ (nb/sr·MeV/c)			
		π^+X^{++}	π^+X°	π^+X^{+-}	$\pi^+X^{\circ\circ}$
	230	23.9±5.4	53.2± 8.9	44.6± 8.0	8.6± 9.3
	250	35.0±6.4	61.1± 9.6	47.9± 8.2	13.3±10.1
	270	27.5±5.8	82.0±10.8	55.5± 8.8	26.5±11.3
	290	40.6±6.6	60.2±10.0	38.6± 7.6	21.6±10.2
	310	30.9±6.1	100.4±11.9	65.1± 9.6	35.3±12.4
	330	31.9±6.1	55.4± 9.6	38.7± 7.7	16.8± 9.8
	350	33.7±6.2	60.6± 8.9	38.9± 7.3	21.8± 9.2
	370	46.3±7.3	52.8± 8.3	33.9± 6.8	18.8± 8.5
	390	53.3±7.8	46.9± 7.7	23.4± 5.8	23.5± 7.8
	410	61.1±8.3	56.5± 8.1	31.5± 6.3	25.0± 8.2
	430	47.3±7.4	55.5± 7.7	28.0± 5.7	27.5± 7.8
	450	35.0±6.2	45.0± 7.4	26.4± 5.7	18.6± 7.5
	470	27.6±5.8	31.2± 6.2	17.3± 4.4	13.9± 6.3
	490	15.5±4.3	33.2± 6.0	17.2± 4.3	16.0± 6.1
	510	16.7±4.3	17.4± 4.4	9.7± 3.1	7.7± 4.5
	530	0.2±1.7	26.5± 5.3	10.6± 3.3	15.8± 5.3
	550		10.0± 3.3	5.2± 2.3	4.7± 3.3
	570		1.0± 1.0		
930	150	28.3±6.8	25.4± 7.3	20.5± 6.3	4.8± 7.4
	170	15.4±5.2	25.3± 6.9	15.4± 5.5	9.9± 7.0
	190	19.6±5.5	37.5± 7.8	31.6± 7.0	6.0± 8.0
	210	22.9±5.9	36.5± 7.8	32.6± 7.0	3.9± 8.1
	230	30.4±6.0	61.5± 9.3	48.6± 8.3	12.9± 9.8
	250	23.3±5.4	59.3± 9.5	38.3± 7.4	21.0± 9.8
	270	31.4±6.1	61.2± 9.7	41.2± 7.6	20.0±10.0
	290	34.0±6.1	68.3±10.4	42.0± 7.9	26.2±10.6
	310	27.2±5.7	73.9±10.5	54.8± 8.8	19.0±11.0
	330	32.0±6.2	61.9± 9.9	47.5± 8.3	14.4±10.3
	350	20.4±5.0	41.4± 7.7	23.8± 5.9	17.6± 7.8
	370	25.5±5.6	60.3± 8.7	26.9± 6.1	33.4± 8.7
	390	32.3±6.2	59.7± 8.4	35.8± 7.0	24.0± 8.6
	410	42.8±7.0	44.8± 7.3	32.7± 6.4	12.1± 7.5
	430	44.5±7.2	55.2± 7.7	30.2± 5.9	25.0± 7.8
	450	46.2±7.2	46.6± 7.5	15.8± 4.5	30.8± 7.4
	470	48.2±7.6	46.5± 7.3	25.1± 5.2	21.4± 7.4
	490	31.3±6.0	32.6± 5.9	19.6± 4.5	13.0± 6.0
	510	13.6±3.9	30.1± 5.6	19.3± 4.4	10.8± 5.7
	530	20.9±5.1	30.5± 5.6	19.5± 4.4	11.0± 5.7
	550	8.5±3.2	12.5± 3.6	3.3± 1.9	9.2± 3.6
	570	3.4±1.9	11.0± 3.2	3.7± 1.9	7.2± 3.2
	590	2.3±1.6	2.8± 1.6	0.9± 0.9	1.8± 1.6

Table 7. Double differential cross sections of pions with respect to the missing mass in the laboratory system at $\theta_\pi = 37° - 51°$.

k (MeV)	M (MeV)	$d^2\sigma/d\Omega dM$ (nb/sr·MeV)			
		π^-X^{++}	π^+X°	π^+X^{+-}	$\pi^+X^{\circ\circ}$
730	1090	9.3± 3.3	39.2± 6.2	18.6± 4.6	20.6± 6.4
	1110	0.3± 2.1	45.9± 6.6	24.6± 5.2	21.3± 6.8
	1130	5.7± 3.0	61.7± 7.7	36.9± 6.5	24.7± 8.2
	1150	11.6± 3.8	85.9± 9.0	54.8± 8.1	31.1± 9.8
	1170	25.8± 5.2	105.8±10.0	54.7± 8.2	51.0±10.7
	1190	52.5± 7.1	126.8±11.4	89.4±10.8	37.5±13.0
	1210	62.1± 7.7	135.2±11.9	78.4±10.1	56.8±13.1
	1230	85.6± 8.8	127.2±11.6	81.7±10.3	45.5±12.9
	1250	83.5± 8.7	120.3±11.2	68.0± 9.4	52.3±12.2
	1270	80.2± 8.8	88.0± 9.9	50.3± 8.1	37.7±10.5
	1290	87.6± 9.4	98.1±10.2	56.1± 8.4	42.1±10.9
	1310	69.0± 9.3	66.0± 9.4	39.3± 7.5	26.7± 9.8
	1330	71.1±10.3	47.7± 8.7	21.9± 6.2	25.8± 8.9
	1350	6.8± 3.2	2.9± 2.7	−0.2± 1.4	3.1± 2.7
770	1090	2.6± 2.5	24.7± 6.4	14.1± 4.1	20.6± 6.5
	1110	5.0± 2.9	40.6± 6.8	28.4± 5.9	12.1± 7.1
	1130	7.8± 3.4	43.9± 6.8	25.3± 5.6	18.7± 7.1
	1150	28.2± 5.9	66.5± 8.3	40.6± 7.1	25.9± 8.8
	1170	31.9± 6.2	65.2± 8.6	34.1± 6.8	31.1± 9.0
	1190	65.0± 8.6	111.5±10.7	68.0± 9.5	43.5±11.8
	1210	60.4± 8.3	112.8±11.3	58.7± 9.1	54.1±12.0
	1230	77.4± 9.3	137.3±12.7	85.0±11.2	52.3±14.1
	1250	65.1± 8.5	128.7±12.4	92.2±11.6	36.6±14.0
	1270	80.5± 9.4	94.8±11.1	47.2± 8.4	47.6±11.6
	1290	76.3± 9.3	108.9±11.4	57.5± 9.2	51.4±12.1
	1310	59.1± 8.6	105.1±11.1	63.4± 9.4	41.7±12.0
	1330	67.6± 9.8	104.5±11.5	46.0± 8.3	58.4±11.9
	1350	70.0±10.8	89.2±11.7	46.3± 8.9	42.9±12.1
	1370	6.8± 3.8	16.9± 5.6	13.9± 5.2	3.0± 5.7
810	1090	1.6± 1.8	15.6± 4.5	6.5± 3.0	9.2± 4.5
	1110	8.3± 3.4	25.8± 5.5	17.5± 4.5	8.3± 5.7
	1130	11.3± 3.8	22.6± 5.4	16.3± 4.5	6.3± 5.6
	1150	17.9± 4.5	37.2± 6.4	16.9± 4.6	20.3± 6.5
	1170	24.3± 5.3	54.0± 7.4	35.5± 6.4	18.5± 7.8
	1190	36.0± 6.2	66.8± 8.5	39.4± 7.1	27.5± 8.9
	1210	70.0± 8.4	78.1± 9.1	46.7± 7.8	31.4± 9.7
	1230	67.3± 8.3	122.8±11.3	67.3± 9.5	55.6±12.2
	1250	61.5± 8.0	95.5±10.8	43.8± 8.0	51.7±11.3
	1270	60.7± 7.9	104.1±11.4	60.0± 9.2	44.1±12.2
	1290	51.5± 7.3	114.8±11.6	73.0±10.0	41.8±12.7
	1310	69.6± 8.4	114.0±11.5	68.0± 9.8	46.0±12.4
	1330	77.9± 9.2	104.8±10.9	51.7± 8.5	53.1±11.5
	1350	46.7± 7.7	78.3±10.0	43.1± 7.9	35.2±10.5
	1370	61.6± 9.7	56.4± 9.9	32.1± 7.6	24.3±10.2
	1390	25.4± 6.6	20.7± 6.5	12.4± 5.0	8.3± 6.5
850	1090	5.0± 2.6	2.7± 0.9	4.3± 2.3	−1.6± 2.9
	1110	5.0± 2.5	16.1± 4.5	5.2± 2.7	10.9± 4.5
	1130	11.6± 3.8	19.4± 4.9	8.7± 3.3	10.7± 5.0
	1150	13.1± 4.1	20.7± 5.3	13.6± 4.1	7.1± 5.3
	1170	17.8± 4.5	42.5± 6.8	28.0± 5.8	14.5± 7.0
	1190	56.1± 7.6	60.0± 7.6	30.6± 6.0	29.4± 7.9

Table 7. (continued)

k (MeV)	M (MeV)	$d^2\sigma/d\Omega dM$ (nb/sr·MeV)			
		π^-X^{++}	π^+X°	π^+X^{+-}	$\pi^+X^{\circ\circ}$
	1210	57.6± 7.7	61.8± 8.0	39.8± 7.0	20.3± 8.5
	1230	59.0± 7.8	85.8± 9.4	52.3± 8.2	33.5±10.1
	1250	61.7± 8.0	94.1± 9.9	56.1± 8.5	38.1±10.7
	1270	49.6± 7.2	90.3±10.5	63.9± 9.4	26.4±11.4
	1290	47.4± 7.1	98.5±11.2	63.4± 9.5	35.1±12.0
	1310	51.9± 7.3	117.4±11.8	90.0±11.1	27.4±13.4
	1330	53.7± 7.5	121.6±11.7	81.7±10.6	39.8±13.1
	1350	63.3± 8.3	92.5±10.4	65.3± 9.5	27.2±11.4
	1370	33.5± 6.7	49.7± 8.7	39.2± 7.5	10.5± 9.1
	1390	62.5± 9.6	53.7± 9.5	37.7± 7.8	16.0± 9.8
	1410	26.8± 7.0	32.4± 7.9	23.7± 6.6	8.7± 8.0
890	1090	6.5± 2.9	10.9± 4.5	8.7± 3.3	2.3± 4.5
	1110	3.8± 2.4	14.8± 4.6	10.2± 3.4	4.7± 4.6
	1130	10.5± 3.5	15.4± 4.4	8.1± 3.1	7.3± 4.4
	1150	18.8± 4.7	25.9± 5.5	14.4± 4.1	11.5± 5.6
	1170	24.5± 5.3	43.2± 6.8	27.9± 5.6	15.3± 7.1
	1190	38.4± 6.4	40.2± 6.7	21.9± 5.1	18.3± 6.9
	1210	52.3± 7.4	63.1± 7.9	38.4± 6.7	24.8± 8.3
	1230	76.9± 8.9	60.3± 7.9	30.5± 6.0	29.8± 8.2
	1250	50.2± 7.3	61.5± 8.3	38.3± 7.1	23.1± 8.8
	1270	49.2± 7.2	63.2± 8.5	36.2± 7.0	27.0± 8.9
	1290	35.0± 6.2	78.6± 9.9	52.2± 8.5	26.4±10.5
	1310	39.6± 6.6	99.5±11.2	75.3±10.4	24.2±12.4
	1330	52.3± 7.3	96.0±11.1	65.0± 9.5	31.0±12.0
	1350	42.9± 6.8	91.4±10.9	64.4± 9.5	27.0±11.8
	1370	40.4± 6.9	90.5±10.5	69.3± 9.8	21.1±11.6
	1390	45.1± 7.5	89.9±10.4	62.1± 9.2	27.9±11.3
	1410	51.3± 8.6	60.1± 9.8	33.7± 7.3	26.4±10.0
	1430	32.3± 7.7	55.8± 9.8	33.9± 8.0	21.9±10.1
	1450	1.4± 1.6	2.8± 2.3	2.4± 2.1	0.4± 2.3
930	1090	3.7± 2.2	0.5± 3.6	3.0± 2.4	−2.4± 3.6
	1110	4.8± 2.5	7.2± 4.0	6.3± 2.9	0.9± 4.1
	1130	17.0± 4.5	12.1± 4.5	9.8± 3.4	2.2± 4.5
	1150	18.2± 4.6	24.9± 5.2	15.3± 4.1	9.6± 5.4
	1170	23.6± 5.2	41.5± 6.5	27.1± 5.6	14.4± 6.8
	1190	43.4± 6.9	34.6± 6.2	21.6± 5.0	13.0± 6.3
	1210	45.9± 7.1	52.0± 7.4	29.6± 5.9	22.4± 7.7
	1230	57.9± 7.8	58.9± 7.6	33.9± 6.3	25.0± 8.0
	1250	44.5± 7.0	61.7± 7.8	40.9± 6.9	20.8± 8.3
	1270	42.8± 6.8	55.5± 7.9	25.0± 5.8	30.5± 8.1
	1290	26.5± 5.6	69.3± 8.7	38.4± 7.1	30.9± 9.1
	1310	28.2± 5.7	59.7± 8.8	35.2± 7.1	24.5± 9.1
	1330	34.2± 6.2	88.7±10.7	78.4±10.5	10.3±12.1
	1350	37.4± 6.4	83.5±10.6	48.8± 8.4	34.7±11.2
	1370	40.3± 6.7	95.5±11.0	76.1±10.2	19.4±12.2
	1390	45.4± 7.2	66.3± 9.6	43.5± 8.0	22.8±10.1
	1410	36.7± 6.9	68.4± 9.4	52.6± 8.5	15.8±10.1
	1430	32.3± 7.2	53.3± 9.2	44.7± 8.1	8.6± 9.7
	1450	37.2± 8.2	38.9± 8.8	21.0± 6.4	17.9± 8.9
	1470	2.7± 2.2	3.9± 3.2	3.9± 2.9	0.0± 3.2

Table 8. Double differential cross sections with respect to the proton momentum in the laboratory system at $\theta_\pi = 37° - 51°$.

k (MeV)	p (MeV/c)	$d^2\sigma/d\Omega dp$ (nb/sr·MeV/c)		
		pX°	pX^{+-}	pX$^{\circ\circ}$
730	330	54.7± 9.9	34.8± 8.2	19.9± 8.7
	350	53.1± 9.7	40.2± 8.5	12.8± 8.2
	370	83.6±10.7	62.8±10.6	20.8± 9.1
	390	75.9±10.2	62.9±10.5	13.0± 8.4
	410	76.4± 9.6	71.3±10.7	5.1± 8.0
	430	76.1± 9.3	58.5± 9.6	17.6± 7.8
	450	78.3± 9.3	77.4±10.9	0.8± 7.2
	470	73.9± 8.9	67.9± 9.9	6.0± 6.6
	490	56.0± 7.7	43.4± 7.7	12.5± 5.6
	510	48.0± 6.9	34.4± 6.7	13.6± 4.9
	530	35.7± 6.0	27.9± 5.6	7.8± 4.0
	550	29.3± 5.3	20.8± 4.9	8.5± 3.5
	570	15.1± 3.9	14.3± 3.8	0.9± 2.0
	590	9.1± 3.2	1.0± 2.2	8.1± 3.0
770	330	65.1±10.7	36.3± 8.7	28.7± 9.5
	350	43.6± 9.1	39.6± 8.4	4.0± 7.5
	370	67.6± 9.9	48.9± 9.4	18.8± 8.4
	390	64.8± 9.6	58.5±10.2	6.3± 7.7
	410	68.6± 9.3	63.1±10.1	5.5± 7.6
	430	70.7± 9.1	60.8± 9.8	9.9± 7.3
	450	64.8± 8.6	58.6± 9.4	6.2± 6.5
	470	76.2± 9.1	63.4± 9.7	12.8± 7.0
	490	56.4± 7.8	48.2± 8.2	8.2± 5.5
	510	58.5± 7.7	50.3± 8.1	8.2± 5.1
	530	48.4± 6.9	39.4± 6.9	9.0± 4.6
	550	40.7± 6.3	31.9± 6.1	8.8± 4.0
	570	21.0± 4.6	18.2± 4.4	2.8± 2.5
	590	18.4± 4.3	12.7± 3.8	5.7± 2.7
	610	10.2± 3.3	2.5± 2.3	7.7± 3.0
	630	4.8± 2.8	4.6± 2.5	0.2± 1.5
810	330	41.3± 8.8	30.2± 7.4	11.2± 7.5
	350	40.8± 8.6	14.7± 6.2	26.1± 8.4
	370	49.1± 8.5	32.9± 7.6	16.3± 7.3
	390	47.1± 8.3	28.8± 7.4	18.3± 7.2
	410	62.3± 8.7	60.9± 9.7	1.4± 7.0
	430	49.5± 7.6	34.8± 7.3	14.7± 6.3
	450	71.8± 8.8	64.8± 9.8	7.0± 6.8
	470	65.8± 8.3	52.0± 8.6	13.9± 6.4
	490	61.1± 8.0	48.7± 8.1	12.4± 5.8
	510	49.4± 7.0	40.7± 7.1	8.7± 4.6
	530	38.2± 6.1	27.9± 5.7	10.3± 4.2
	550	43.3± 6.3	32.2± 6.0	11.1± 4.2
	570	34.3± 5.5	26.7± 5.3	7.7± 3.5
	590	21.0± 4.4	15.4± 4.0	5.5± 2.7
	610	23.6± 4.6	17.9± 4.2	5.6± 2.8
	630	11.0± 3.5	9.0± 3.1	2.0± 2.0
	650	5.7± 2.4	3.0± 2.0	2.7± 1.6
850	330	37.2± 8.6	22.3± 6.7	14.9± 7.7
	350	32.0± 8.2	22.5± 6.6	9.5± 7.2
	370	32.5± 7.4	19.6± 6.1	12.9± 6.7
	390	47.5± 8.4	34.4± 7.8	13.1± 7.0

Table 8. (continued)

k (MeV)	p (MeV/c)	$d^2\sigma/d\Omega dp$ (nb/sr·MeV/c)		
		pX°	pX^{+-}	pX°°
	410	48.6± 7.9	31.5± 7.1	17.1± 7.0
	430	42.5± 7.2	35.1± 7.2	7.4± 5.8
	450	44.2± 7.1	33.4± 7.0	10.8± 5.6
	470	41.7± 6.8	41.2± 7.4	0.5± 4.6
	490	47.0± 7.1	36.6± 7.0	10.4± 5.1
	510	55.9± 7.4	49.1± 7.9	6.8± 4.8
	530	42.6± 6.4	35.6± 6.3	7.0± 4.1
	550	43.2± 6.3	34.2± 6.2	9.1± 4.0
	570	38.8± 5.9	30.6± 5.7	8.2± 3.7
	590	49.2± 6.6	40.0± 6.5	9.2± 4.0
	610	36.7± 5.7	27.7± 5.3	8.9± 3.6
	630	16.7± 4.1	10.4± 3.5	6.4± 2.9
	650	8.7± 2.9	4.2± 2.3	4.5± 2.1
	670	9.6± 3.0	4.6± 2.4	5.0± 2.3
890	330	39.9± 8.8	20.1± 6.6	19.8± 8.2
	350	35.5± 8.5	22.9± 6.8	12.7± 7.5
	370	50.7± 8.7	30.4± 7.5	20.2± 7.7
	390	43.4± 8.2	33.0± 7.7	10.4± 6.8
	410	54.3± 8.3	42.8± 8.2	11.5± 7.0
	430	38.4± 7.0	28.4± 6.6	10.1± 5.8
	450	46.4± 7.3	44.7± 8.0	1.7± 5.3
	470	52.3± 7.6	42.7± 7.7	9.6± 5.6
	490	43.8± 6.9	37.4± 7.1	6.4± 4.7
	510	48.2± 7.0	40.4± 7.1	7.8± 4.6
	530	39.2± 6.2	32.7± 6.1	6.6± 4.0
	550	42.2± 6.3	32.7± 6.1	9.4± 4.1
	570	45.7± 6.4	37.5± 6.4	8.2± 4.0
	590	36.2± 5.7	27.3± 5.4	8.9± 4.1
	610	36.8± 5.8	24.9± 5.2	11.9± 4.0
	630	31.3± 5.5	24.8± 5.1	6.5± 3.6
	650	26.4± 4.9	20.0± 4.6	6.4± 3.9
	670	17.9± 4.1	12.9± 3.6	5.0± 3.2
	690	8.3± 2.8	4.9± 2.2	3.4± 2.8
	710	7.8± 2.6	6.1± 2.4	1.7± 2.5
930	330	36.3± 8.5	12.5± 5.8	23.8± 8.4
	350	31.3± 8.1	12.2± 5.8	19.1± 7.8
	370	41.3± 8.1	30.5± 7.3	10.9± 6.9
	390	38.6± 7.8	28.7± 7.2	9.9± 6.6
	410	35.1± 7.0	22.4± 6.0	12.8± 6.3
	430	33.3± 6.6	27.9± 6.4	5.4± 5.3
	450	35.8± 6.6	34.6± 7.0	1.2± 4.7
	470	40.2± 6.8	32.2± 6.7	8.1± 5.0
	490	51.0± 7.4	39.6± 7.3	11.4± 5.3
	510	47.0± 6.9	36.3± 6.8	10.7± 4.7
	530	44.8± 6.6	39.6± 6.7	5.2± 4.1
	550	40.3± 6.2	33.6± 6.1	6.7± 3.7
	570	51.2± 6.8	45.8± 7.1	5.3± 4.0
	590	46.3± 6.4	37.7± 6.4	8.6± 3.9
	610	30.4± 5.2	26.6± 5.1	3.8± 2.8
	630	34.8± 5.7	26.6± 5.3	8.2± 3.5
	650	29.3± 5.1	26.7± 5.2	2.6± 2.3
	670	18.5± 4.1	15.4± 3.9	3.1± 2.1
	690	23.6± 4.6	22.2± 4.6	1.4± 1.9
	710	11.0± 3.1	6.4± 2.6	4.6± 2.2
	730	4.0± 1.2	0.3± 0.9	3.7± 2.0

Table 9. Double differential cross sections of protons with respect to the missing mass in the laboratory system at $\theta_\pi = 37° - 51°$.

k (MeV)	M (MeV)	$d^2\sigma/d\Omega dM$ (nb/sr·MeV)		
		pX^0	pX^{+-}	pX^{00}
730	290	24.9± 4.9	19.1± 4.5	5.8± 3.1
	310	54.3± 6.9	36.9± 6.3	17.5± 5.0
	330	82.0± 8.5	61.5± 8.3	20.5± 6.2
	350	86.2± 9.1	72.3± 9.3	13.9± 6.5
	370	123.4±11.1	99.6±11.9	23.9± 9.7
	390	167.9±13.1	134.4±15.6	33.5±13.1
	410	140.9±13.0	106.3±14.2	34.5±12.7
	430	90.4±10.8	63.6±10.5	26.8±10.1
	450	10.7± 3.8	9.2± 3.5	1.6± 3.0
770	290	24.4± 4.9	16.2± 4.2	8.2± 3.6
	310	45.8± 6.5	26.8± 5.5	19.0± 5.0
	330	55.7± 7.1	35.9± 6.4	19.8± 5.3
	350	74.7± 8.3	59.3± 8.4	15.4± 5.9
	370	91.8± 9.4	78.4±10.2	13.4± 7.3
	390	136.3±11.8	125.2±14.6	11.1±11.0
	410	151.9±12.9	127.4±15.6	24.5±12.7
	430	131.9±12.9	103.4±14.1	28.5±12.5
	450	70.3±10.1	58.4±10.0	11.9± 9.0
	470	7.1± 3.3	2.7± 2.4	4.5± 3.1
810	290	17.7± 4.2	12.2± 3.5	5.5± 2.9
	310	36.7± 5.7	23.4± 5.0	13.4± 4.2
	330	46.6± 6.4	33.0± 5.9	13.5± 4.5
	350	61.2± 7.2	52.3± 7.4	8.9± 4.7
	370	63.1± 7.6	53.9± 8.0	9.2± 5.4
	390	79.0± 8.7	68.3± 9.9	10.7± 7.1
	410	96.8±10.1	73.9±11.0	22.9± 9.2
	430	120.3±11.5	101.5±13.3	18.8±10.8
	450	122.3±12.2	80.6±12.4	41.7±11.8
	470	70.5± 9.7	44.2± 8.8	26.3± 9.2
	490	3.3± 2.3	5.5± 2.5	−2.3± 1.3
850	290	15.0± 4.1	7.2± 2.9	7.8± 3.6
	310	28.7± 5.1	22.1± 4.6	6.6± 3.5
	330	31.5± 5.4	20.7± 4.6	10.8± 3.9
	350	51.4± 6.7	42.2± 6.6	9.2± 4.4
	370	64.4± 7.4	56.6± 8.0	7.8± 5.2
	390	69.1± 7.9	66.8± 9.4	2.3± 6.1
	410	82.5± 8.9	73.0±10.5	9.6± 7.5
	430	104.3±10.5	78.8±11.4	25.4± 9.7
	450	78.3±10.1	56.9± 9.8	21.3± 9.2
	470	74.5±10.6	66.0±10.7	8.5± 9.4
	490	70.2± 9.7	43.9± 8.7	26.3± 9.0
	510	1.6± 1.7	0.2± 1.1	1.4± 1.7
890	290	6.4± 3.5	9.2± 3.0	−2.8± 2.2
	310	24.8± 5.1	19.8± 4.4	5.0± 3.6
	330	33.3± 5.6	31.2± 5.4	2.1± 3.3
	350	47.6± 6.5	41.8± 6.5	5.8± 4.2
	370	53.4± 6.9	48.3± 7.4	5.1± 4.6
	390	62.9± 7.5	54.8± 8.5	8.1± 5.7
	410	69.7± 8.1	57.8± 9.1	11.9± 6.6
	430	85.7± 9.3	74.7±10.8	11.0± 8.0
	450	88.5±10.1	72.7±11.0	15.8± 8.9

Table 9. (continued)

k (MeV)	M (MeV)	$d^2\sigma/d\Omega dM$ (nb/sr·MeV)		
		pX°	pX^{+-}	$pX^{\circ\circ}$
	470	104.5±11.3	75.7±11.6	28.7±10.6
	490	94.2±11.5	61.1±10.8	33.1±10.9
	510	49.7± 8.5	40.7± 8.1	8.9± 7.4
	530	1.0± 1.2	0.7± 1.0	0.3± 1.0
930	290	4.0± 2.8	3.8± 2.0	0.2± 2.4
	310	20.9± 4.8	25.6± 4.8	−4.7± 2.3
	330	23.1± 5.0	24.6± 4.9	−1.4± 2.9
	350	39.1± 6.1	35.8± 5.9	3.3± 3.9
	370	40.8± 6.1	39.9± 6.5	0.8± 3.9
	390	58.7± 7.2	62.6± 8.8	−3.8± 5.2
	410	45.6± 6.5	47.3± 7.8	−1.6± 4.6
	430	66.2± 7.9	61.2± 9.3	4.9± 6.3
	450	76.7± 9.0	70.3±10.3	6.4± 7.6
	470	89.6±10.2	75.1±11.1	14.5± 9.0
	490	105.2±11.4	82.4±12.0	22.8±10.6
	510	72.8±10.6	42.9± 9.2	29.9±10.1
	530	47.3± 7.9	19.7± 6.2	27.6± 7.8
	550	0.7± 0.8	−0.2± 0.2	0.8± 1.0

(c) Although there is a peak of Δ° in $\pi^+X^{\circ\circ}$ spectra (Figs. 38), there seems no clear peak in π^+X° spectra (Figs. 36) and π^+X^{+-} spectra (Figs. 37). Small contribution of Δ° in the last two spectra can be attributed to the following two reasons: The first, since there is a large contribution due to the π^+ from the decay $\pi^-\Delta^{++}\to\pi^+\pi^-p$ in the reaction $\gamma p\to\pi^-\Delta^{++}$, Δ° peak become obscure; the second the decay branching ratios of Δ° to π^-p and to $\pi^\circ n$ is 1 : 2.

(d) There are large discrepancies between the present results and Fukui *et al.*'s at around the peak of Δ for both of the spectra of the positive and negative pions. They measured momentum spectra at $\theta_\pi^{Lab.}=40^\circ\pm2^\circ$ by the photon subtraction method in 100 MeV step. These discrepancies can not be explained by the differences of the kinematical setting in angle and energy width of the incident photons of the two experiment. In the lower momentum region, the results of the two experiments are consistent each other.

(e) The shape of the spectra of $pX^{\circ\circ}$ (Figs. 41) are very different from that of pX^{+-} (Figs. 40). These differences seems to come from two sources: the first, the cross section of the reaction $\gamma p\to p\pi^\circ\pi^\circ$ is smaller than that of the reaction $\gamma p\to p\pi^+\pi^-$; the second, the triple pion photoproduction of $\gamma p\to p\pi^\circ\pi^\circ\pi^\circ$ is included in $pX^{\circ\circ}$. More quantitative interpretations are given in the successive section.

The measurements of the cross sections of the single pion photoproduction reactions $\gamma p\to\pi^+n$ and $\gamma p\to\pi^\circ p$ were measured at the same time[26] as an overall check of our detection system and the method of the reduction of the cross sections. The cross sections are shown in Fig. 42. The results are in good agreement with that of the previous experiments.

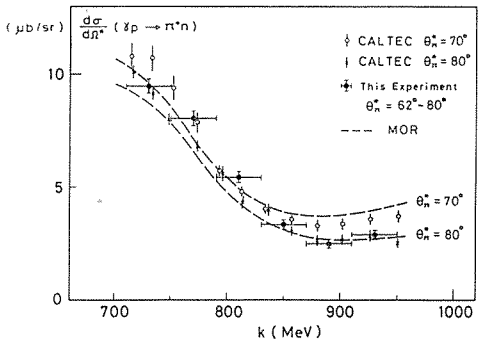

Fig. 42-a

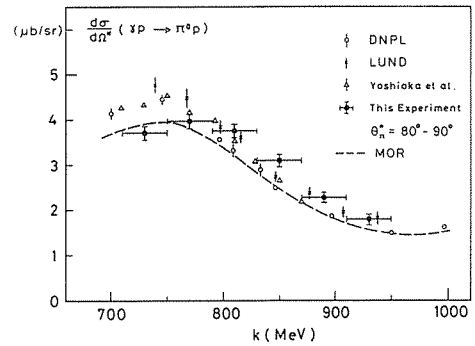

Fig.42-b

Figs. 42. (a) Differential cross sections of $\gamma p \to \pi^+ n$ at a c.m. angle $\theta_\pi^* = 60°$. The present results (closed circles) are plotted together with the data by Eckland and Walker[29] (open circles and crosses). Solid lines show the results of the phenomenological analysis by MOR[30] (Moorhouse, Overlack, and Rosenfeld). (b) Differential cross sections of $\gamma p \to \pi^0 p$ at a c.m. angle $\theta_\pi^* = 90°$. The present results (closed circles) are plotted together with the results by Barton et al.[31] (open circles), Dougan et al.[32] (crosses), and Yoshioka et al.[33] (triangles). Solid line shows the result of the analysis by MOR.

VI-2. Fitting of the Spectrum

(1) *Shape functions*

The momentum spectra of pions and protons can be described as

$$\frac{d^2\sigma}{d\Omega dp_1} = \frac{(2\pi)^4}{4km_p} \cdot \frac{{p_1}^2}{(2\pi)^3 2E_1} \int \frac{d^3p_2}{(2\pi)^3 2E_2} \cdot \frac{d^3p_3}{(2\pi)^3 2E_3} \cdot \delta^4(P_f - P_i) \cdot |T_{fi}|^2, \qquad \text{(VI-1)}$$

where

(E_1, P_1); energy and momentum of the particle observed by the spectrometer,

(E_j, P_j); $j=2, 3$ energy and momentum of the particle which was not observed by the spectrometer,

$\delta^{(4)}(P_f - P_i)$; conservation of four momentum,

T_{fi} ; transition amplitude.

The double pion photoproduction reactions are supposed to be consists of the dominant quasi-two body reactions $\gamma p \to \pi \Delta$ and the three body invariant phase space production. Then the transition amplitude decomposed into three parts in the present photon energy region,

$$T_{fi} = T_0 + T_1 + T_2. \qquad \text{(VI-2)}$$

T_0 represents the contribution from three body phase space production. The amplitude T_1 related to the recoil pions of the quasi-two body reaction $\gamma p \to \pi \Delta$, and the amplitude T_2 related to pions or protons from the decay of Δ. Each of these amplitudes is parametrized with the phenomenological approach according to Jackson,[27]

$$T_0 = a_0,$$
$$T_1 = a_1 e^{i\delta_1} \sin\delta_1 / \sqrt{M_0 \Gamma(M_1)},$$
$$T_2 = a_2 e^{i\delta_2} \sin\delta_2 / \sqrt{M_0 \Gamma(M_2)}, \qquad \text{(VI-3)}$$

$$\delta_j=\tan^{-1}\{M_0\Gamma(M_j)/(M_0^2-M_j^2)\} \quad (j=1, 2),$$
$$\Gamma(M)=\Gamma_0\cdot(p'/p_r')^3\cdot(\rho/\rho_r),$$
$$\rho=\{(M+m_p)^2-\mu^2\}/M^2,$$

where

M_0, Γ_0; mass and width of Δ, respectively,
M_j ; missing mass of the spectrometer particle,
p' ; three momentum of the unobserved particle in the rest system of the missing mass particle,
p_r', ρ_r ; subscript r denotes the quantities evaluated at the Δ mass.

The observed cross sections can be expanded, using the functions g_i ($i=0,\ldots, 3$), in the followings;

$$\frac{d^3\sigma}{d\Omega dp}=\sum_{i=0}^{3}B_i(k)g_i(k, p), \tag{VI-4}$$

where the shape functions g_0, g_1, and g_2 are defined as follows,

$$g_0(k, p)=\frac{\pi p_1^2 p'}{2E_1M_1},$$
$$g_1(k, p)=\frac{\pi p_1^2 p'}{2E_1M_1}\cdot\frac{\sin^2\delta_1}{M_0\Gamma(M_1)}, \tag{VI-5}$$
$$g_2(k, p)=\frac{\pi p_1^2 p'}{2E_1M_1}\cdot\int_0^1 d\cos\theta_2\frac{\sin^2\delta_2}{M_0\Gamma(M_2)},$$

The integration of the last equation (VI–5) was carried out with respect to Δ rest system. The functions g_0, g_1, and g_2 come from the calculations of $|T_0|^2$, $|T_1|^2$, and $|T_2|^2$ in formula (VI–1), respectively. All the three interference terms among T_0, T_1, and T_2 are neglected for easiness of treatment. There is no effect of the reaction $\gamma p\to\rho N$ because the photon energy was below the threshold of this reaction. The triple pion photoproduction process $\gamma p\to\pi\pi\pi N$ are taken into account in the shape function g_3 which corresponds to a four body phase space. The coefficients B_0, B_1, B_2, and B_3 are the parameters to be determined by the fitting of the spectra.

The observed cross sections expressed by the missing mass were also expressed in a similar way as the equation (VI–4),

$$\frac{d^2\sigma}{d\Omega dM}=\sum_{i=0}^{3}B_i^M(k)g_i^M(k, M), \tag{VI-6}$$

where g_i^M, ($i=0,\ldots, 3$) are shape functions and B_i^M, ($i=0,\ldots, 3$) are the parameters to be determined.

The shape functions g_i and g_i^M, ($i=0,\ldots, 3$) were calculated for pions and protons separately, and typical examples for pions are shown in Figs. 43.

A list of the contributing processes to each final state is given in Table 10.

(2) *Fitting procedure*

Using the shape functions described in the preceding section, a least square fit to the experimental spectrum was performed for each reaction. Since two shape functions g_0 and g_2 are very similar for proton spectra, a fitting with two parameters was made for the spectra. The fitted curves are shown in Figs. 35~41.

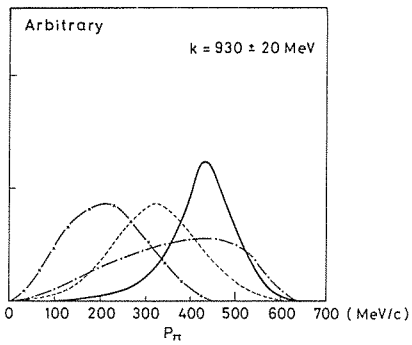

Fig. 43-a

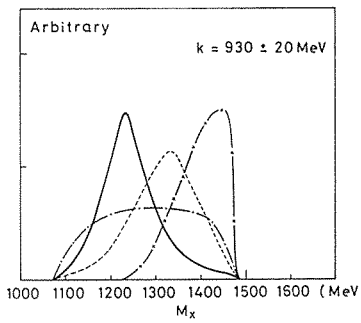

Fig. 43-b

Fig. 43. Shape functions at $k=930$ MeV for (a) pion momentum spectrum and (b) missing mass spectrum associated with pion. Solid line, dashed line, dash-dotted line, and line with crosses correspond to recoil, decay, three-body phase space, and four-body phase space, respectively.

Table 10. List of reactions contributing to the final states.

Final State	Recoil	Decay	Phase Space
$\pi^-+\pi^++p$	$\pi^-+\pi^{++}$	$\pi^++\Delta^\circ$ $\quad\hookrightarrow\pi^-+p$	$\pi+\pi+N$
$\pi^++\pi^-+p$	$\pi^++\Delta^\circ$ $\quad\hookrightarrow\pi^-+p$	$\pi^-+\Delta^{++}$	$\pi+\pi+N$
$\pi^++\pi^\circ+n$	$\pi^++\Delta^\circ$ $\quad\hookrightarrow\pi^\circ+n$	$\pi^\circ+\Delta^+$ $\quad\hookrightarrow\pi^++n$	$\pi+\pi+N$
$p+\pi^++\pi^-$	No	$\pi^++\Delta^\circ$ $\quad\hookrightarrow\pi^-+p$ $\pi^-+\Delta^{++}$	$N+\pi+\pi$
$p+\pi^\circ+\pi^\circ$	No	$\pi^\circ+\Delta^+$ $\quad\hookrightarrow\pi^\circ+p$	$N+\pi+\pi$

VI-3. Results of the Fitting

The cross sections of the reactions $\gamma p \to \pi^- \Delta^{++}$, $\gamma p \to \pi^+ \Delta^\circ$, $\gamma p \to p\pi^\circ\pi^\circ$, and $\gamma p \to p\pi^+\pi^-$ were reduced with the fitting described in the preceding section.

Pion

The differential cross sections of the reactions $\gamma p \to \pi^- \Delta^{++}$ and $\gamma p \to \pi^+ \Delta^\circ$ at a c.m. angle $\theta_\pi^* = 75^\circ \pm 10^\circ$ were obtained in the following was by integrating the recoil term g_1;

$$\frac{d\sigma}{d\Omega^*}(\gamma p \to \pi\Delta) = J \cdot \int B_1(k) \cdot g_1(k, p) dp, \qquad \text{(VI-7)}$$

where

$$J = \frac{\partial\Omega}{\partial\Omega^*}.$$

The obtained cross sections $d\sigma/d\Omega^*(\gamma p \to \pi^- \Delta^{++})$ are listed in Table 11 and shown in Fig. 44. The results are in good agreement with that of Allaby *et al.*[5] and Hauser.[6] The data by ABBHHM[3] also agree with the present ones except one experimental point at $k=700$–800 MeV. But there are disagreements between the

Table 11. Center of mass cross sections of $\gamma p \to \pi^- \Delta^{++}H$ and $\gamma p \to \pi^+ \Delta H^\circ$. R is defined by equation (VI–9) in the text.

k (MeV)	$d\sigma/d\Omega^*(\gamma p \to \pi^- \Delta^{++}H)$ (μb/sr)	$d\sigma/d\Omega^*(\gamma p \to \pi^+ \Delta H^\circ)$ (μb/sr)	R
730±20	4.88±0.89	1.19±0.58	0.24±0.13
770±20	4.23±0.78	2.16±1.27	0.51±0.31
810±20	3.30±0.94	0.93±0.43	0.28±0.15
850±20	3.67±0.62	1.67±1.27	0.46±0.35
890±20	4.56±0.21	1.24±0.52	0.27±0.11
930±20	3.49±0.20	1.40±0.67	0.40±0.19

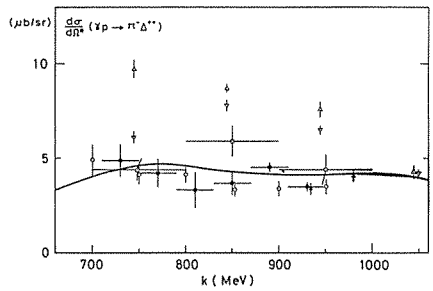

Fig. 44

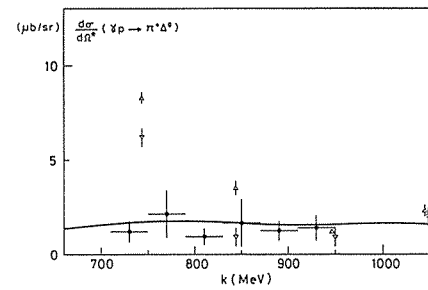

Fig. 55

Figs. 44. Differential cross sections of $\gamma p \to \pi^- \Delta^{++}$ at a c.m. angle $\theta_\pi^* = 75^\circ \pm 10^\circ$. The present results (closed circles) are plotted together with the data by Allaby *et al.*[5] (open circles), Hauser[6] (crosses), ABBHHM[3] (squares), and Fukui *et al.*[8] (upward and downward triangles). The solid line shows the result of the analysis made by Sasaki with $\lambda = 1.2$ GeV^{-2}.

Fig. 45. Differential cross sections of $\gamma p \to \pi^+ \Delta^\circ$ at a c.m. angle $\theta_\pi^* = 75^\circ \pm 10^\circ$. The present results (closed circles) are plotted together with the data by Fukui *et al.*[8] (upward and downward triangles). The solid line shows the result of the analysis made by Sasaki with $\lambda = 1.2$ GeV^{-2}.

present results and Fukui *et al.*'s[8] by the factor of about two. This disagreement is not due to the method of the extraction of $\gamma p \to \pi^- \Delta^{++}$ from the obtained spectra of negative pions, because the same size of difference was already seen in the Δ^{++} peak region in the momentum spectra in Fig. 36–a. Although the present data show a rather flat dependence to the photon energy, Fukui *et al.*'s show a quite different dependence comparing with the present results.

Sasaki[18] used the GIOPE model with the s-channel resonances $P_{11}(1460)$, $D_{13}(1525)$, $S_{11}(1550)$, $F_{15}(1688)$, and $D_{15}(1670)$ in the analysis of the reaction $\gamma p \to \pi \Delta$. The absorption correction at the $\pi N \Delta$ vertex with the following form was assumed;

$$F(t) = \exp\{\lambda(t - \mu^2)\}, \qquad \text{(VI–8)}$$

t; momentum transfer squared

where λ was taken 0.8 GeV^{-2}. However, the value of 1.2 GeV^{-2} for λ gave a better fit to the present results, we used 1.2 GeV^{-2} instead of 0.8 GeV^{-2} in our analysis.

Generally a large amount of the contribution of the positive pions from the decay of $\Delta^{++} \to \pi^+ p$ in the reaction $\gamma p \to \pi^- \Delta^{++}$ makes it difficult to extract the events of $\gamma p \to \pi^+ \Delta^\circ$ as stated in section VI–1. But for the positive pion spectra associated with no charged particles, rather small contribution from the reaction $\gamma p \to \pi^\circ \Delta^+$ exist as seen in Figs. 38. So the cross sections of the reaction $\gamma p \to \pi^+ \Delta^\circ$ (Fig. 45) were de-

termined from the fittings of the $\gamma p \to \pi^+ X^{\circ\circ}$ spectra. Obtained values are listed in Table 11. Although about the same size of the cross sections for $\gamma p \to \pi^+ \Delta^\circ$ were obtained from the fittings of the spectra $\gamma p \to \pi^+ X^\circ$ and $\gamma p \to \pi^+ X^{+-}$, those values were very sensitive to the fitting conditions. Therefore the cross sections obtained from $\pi^+ X^{\circ\circ}$ spectra are more reliable than the ones from $\pi^+ X^\circ$ spectra and $\pi^+ X^{+-}$ spectra.

The cross sections thus obtained are consistent with the ones by Fukui *et al.* above $k=800$ MeV, but at $k=744$ MeV their cross section contradict to our flat behavior in the photon energy. Sasaki's analysis reproduces the present data very well as shown in Fig. 45. The ratio

$$R = \frac{d\sigma/d\Omega^*(\gamma p \to \pi^+ \Delta^\circ)}{d\sigma/d\Omega^*(\gamma p \to \pi^- \Delta^{++})}, \qquad \text{(VI-9)}$$

is very interesting to investigate the reaction mechanism of $\gamma p \to \pi \Delta$. R is calculated for the following cases,

$$R = \begin{cases} 1/3 \text{ if only } I_s = 1/2 \text{ resonance exists in s-channel,} \\ 4/3 \text{ if only } I_s = 3/2 \text{ resonance exists in s-channel,} \\ \sim 1/3 \text{ for GIOPE model,} \end{cases}$$

where I_s denotes s-channel isospin. The ratio obtained from the present experiment at about 40° in the laboratory angle are also listed in Table 11 and shown in Fig. 46 together with the ratios by Fukui *et al.* The ratios by ABBHHM for the total cross section are also shown in this figure for comparison. Very small values of ABBHHM, which is less than 1/3, could not be expected from any model. Fukui *et al.*'s may indicate that there is some change of the reaction mechanism between above and below $k=800$ MeV. The present results show a flat behavior in the photon energy and give a mean value of $R=0.30\pm0.06$. This value and the behavior favor to the GIOPE model and/or $I_s=1/2$ resonances contribution to the reaction $\gamma p \to \pi^- \Delta^{++}$ and $\gamma p \to \pi^+ \Delta^\circ$. The present data are well reproduced by Sasaki's analysis.

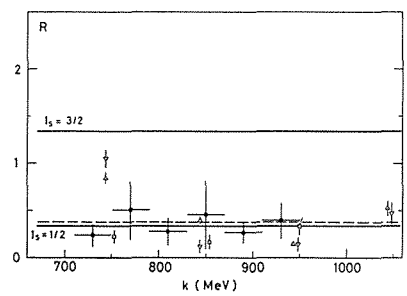

Fig. 46. Ratios of the differential cross sections of $\gamma p \to \pi^+ \Delta^\circ$ to that of $\gamma p \to \pi^- \Delta^{++}$. The present results (closed circles) are shown together with the data by Fukui *et al.*[8] (upward and downward triangles). The ratios of the two reactions with respect to the total cross sections measured by ABBHHM[3] are also shown (squares). Two solid lines correspond to the calculated ratios for s-channel isospin 1/2 and 3/2, and the dashed line is the result of the analysis by Sasaki with $\lambda=1.2$ GeV^{-2}.

Proton

By detecting protons in the spectrometer, two reactions, $\gamma p \to p\pi^\circ\pi^\circ$ and $\gamma p \to p\pi^+\pi^-$ were studied. In the analysis of these reactions, the following integrated cross sections was defined in the laboratory system,

$$\frac{d\sigma}{d\Omega}(\gamma p \to p(\pi\pi)) = \int \frac{d^2\sigma}{d\Omega dp} \cdot dp. \qquad \text{(VI-10)}$$

The results are listed in Table 12 and shown in Fig. 47.

The flat behavior of the cross sections of $\gamma p \to p(\pi^+\pi^-)$ as a function of the incident photon energy is expected from the flat behavior of the dominant reactions $\gamma p \to \pi^- \Delta^{++}$ and $\gamma p \to \pi^+ \Delta^\circ$.

The behavior of the cross sections of $\gamma p \to p(\pi^\circ\pi^\circ)$ shows a broad peak at around the second resonance and diminished to almost 0 at $k=930$ MeV. This behavior may indicate that the s-channel resonances in the second resonance region contribute to this reaction. As seen in Table 10, among three quasi-two body reactions of $\gamma p \to \pi\Delta$, only the reaction $\gamma p \to \pi^\circ \Delta^+$, which has a little contribution from the Born amplitudes, can lead to the final state of $p\pi^\circ\pi^\circ$. The following reaction mechanism may explain the behavior of the cross sections of $\gamma p \to p(\pi^\circ\pi^\circ)$;

$$\gamma p \to I_s = 1/2 \text{ Resonances} \to \pi^\circ \Delta^+ \to \pi^\circ\pi^\circ p.$$

A ratio R' defined as follows;

Table 12. Laboratory cross sections of $\gamma p \to p(\pi\pi)$, $\gamma p \to p(\pi^+\pi^-)$, and $\gamma p \to p(\pi^\circ\pi^\circ)$. R'' is defined by equation (VI-11) in the text.

k (MeV)	$d\sigma/d\Omega$ (μb/sr)			R''
	$\gamma p \to p(\pi\pi)$	$\gamma p \to p(\pi^+\pi^-)$	$\gamma p \to p(\pi^\circ\pi^\circ)$	
730±20	14.26±0.55	10.66±0.56	3.03±0.45	0.28±0.04
770±20	14.39±0.57	10.56±0.55	3.07±0.45	0.29±0.05
810±20	12.68±0.54	9.68±0.55	2.66±0.43	0.27±0.05
850±20	12.06±0.56	9.29±0.56	2.08±0.43	0.22±0.05
890±20	12.62±0.59	10.80±0.62	1.45±0.43	0.13±0.04
930±20	11.18±0.58	10.77±0.62	0.02±0.30	0.00±0.03

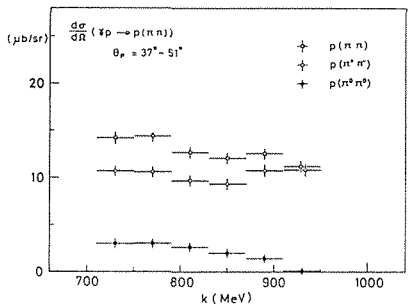

Figs. 47. Obtained laboratory cross sections of $\gamma p \to p(\pi^\circ\pi^\circ)$, $\gamma p \to p(\pi^+\pi^-)$, and $\gamma p \to p(\pi\pi)$ at a laboratory angle $\theta_p = 44^\circ \pm 7^\circ$.

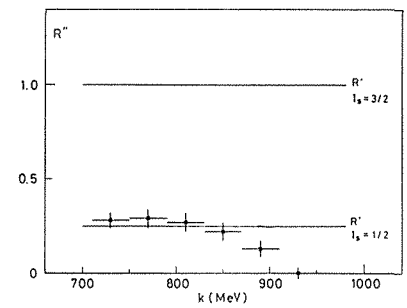

Fig. 48. The ratio R'' at a laboratory angle $\theta_p = 44^\circ \pm 7^\circ$.

$$R' = \frac{\frac{d\sigma}{d\Omega}(\gamma p \to \pi^\circ \Delta^+ \to p(\pi^\circ\pi^\circ))}{\frac{d\sigma}{d\Omega}(\gamma p \to \pi\Delta \to p(\pi^+\pi^-))}, \qquad \text{(VI-11)}$$

is useful for the selection of models as well as R. Namely,

$$R' = \begin{cases} 0.25 \text{ if only } I_s = 1/2 \text{ resonance exists in s-channel,} \\ 1 \text{ if only } I_s = 3/2 \text{ resonance exists in s-channel,} \\ \sim 0 \text{ for GIOPE model.} \end{cases}$$

Since the extraction of $\gamma p \to \pi\Delta$ from the present measurement is difficult, the following R'' is defined in order to analyze the present results;

$$R'' = \frac{\frac{d\sigma}{d\Omega}(\gamma p \to p(\pi^\circ\pi^\circ))}{\frac{d\sigma}{d\Omega}(\gamma p \to p(\pi^+\pi^-))}. \qquad \text{(VI-12)}$$

The obtained ratios are listed in Table 12 and shown in Fig. 48.

The difference between R' and R'' lies in the contribution of the phase space production which is included in R''. Each of the cross section of $\gamma p \to p(\pi^\circ\pi^\circ)$ and $\gamma p \to p(\pi^+\pi^-)$ can be assumed to be the sum of the cross section due to phase space production and the quasi-two body reaction of $\gamma p \to \pi\Delta$. For the phase space production, the ratio of cross section of $\gamma p \to p\pi^\circ\pi^\circ$ to that of $\gamma p \to p\pi^+\pi^-$ is calculated to be 2/3 from the statistical model by Shapiro.[28] By using the above assumptions and a parameter α, which is a ratio of cross section contributed from the phase space production to that from the quasi-two body reaction $\gamma p \to \pi\Delta$ for $\gamma p \to p\pi^+\pi^-$, a relation between R' and R'' is obtained from equations (VI-11) and (VI-12);

$$R' = (1+\alpha)R'' - \frac{2}{3}\alpha.$$

As the values of R'' are less than 0.3 in this experiment, R'' gives the upper limit of R' independently of the value of α.

Then our data of R'' (Fig. 48) indicate that the quasi-two body reaction $\gamma p \to \pi\Delta$ is dominated by the GIOPE and/or $I_s = 1/2$ resonances contribution in the second resonance region and the reaction is dominated by the GIOPE at around $k = 900$ MeV.

The $\gamma p \to p\pi^\circ\pi^\circ$ reaction has been measured by two groups. Kitagaki *et al.*[11] measured the reaction by detecting a proton and a photon from the decay of the neutral pions at a fixed laboratory angle. They obtained total cross sections of the reaction from their data by assuming the shape of the incident photon energy dependence and the phase space production. Their cross section is very small below 650 MeV. The cross sections, however, increase steeply with the photon energy and have a value of about 20 μb at 900 MeV and about 40 μb at 1000 MeV. These large cross sections above 900 MeV are not compatible with the present results. Beneventano *et al.*[10] also measured the cross sections for photon energies between 600 MeV and 900 MeV for five proton momenta and at a laboratory angle $\theta_p = 32°$. Their data do not contradict to the present results.

Deviations of the experimental data from the fitted curves in the spectra of

$\gamma p \to pX^{\circ}$ (Figs. 39) and $\gamma p \to pX^{+-}$ (Figs. 40) for $k=730$ MeV, $k=770$ MeV, and $k=810$ MeV are seen in the present analysis. The origin of the deviations has not been found.

VI-4. Contribution of the s-channel Resonance to $\gamma p \to \pi \Delta$

The contribution of the s-channel resonances to the reaction $\gamma p \to \pi \Delta$ is discussed in this section.

In this discussion the amplitudes of the reaction $\gamma p \to \pi \Delta$ were assumed to consist of a coherent sum of the GIOPE amplitude and the s-channel resonances amplitudes. GIOPE model introduced by Stichel and Scholtz[13] consists of four graphs as shown in Fig. 49. Using the four amplitudes H^{I}, H^{II}, H^{III}, and H^{IV} corresponding to each graph of the GIOPE model for a full isospin, the following amplitudes are written down for the three reactions;

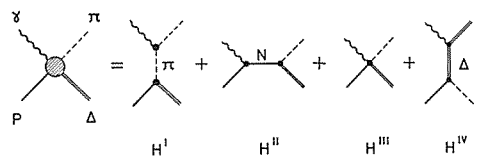

Fig. 49. Four GIOPE graphs.

$$
\begin{aligned}
H^{++} &\equiv H(\gamma p \to \pi^{-} \Delta^{++}) = -H^{I} + H^{II} - H^{III} + 2H^{IV}, \\
H^{+} &\equiv H(\gamma p \to \pi^{\circ} \Delta^{+}) = -\sqrt{\frac{2}{3}} (H^{II} + H^{IV}), \\
H^{\circ} &\equiv H(\gamma p \to \pi^{+} \Delta^{\circ}) = \sqrt{\frac{1}{3}} (H^{I} + H^{II} + H^{III}).
\end{aligned}
\tag{VI-13}
$$

The resonance amplitudes can be decomposed into s-channel isospin amplitudes as follows;

$$
\begin{aligned}
A^{++} &\equiv A(\gamma p \to \pi^{-} \Delta^{++}) = \sqrt{\frac{1}{2}} A_{1/2} + \sqrt{\frac{2}{5}} A_{3/2}, \\
A^{+} &\equiv A(\gamma p \to \pi^{\circ} \Delta^{+}) = -\sqrt{\frac{1}{3}} A_{1/2} + \sqrt{\frac{1}{15}} A_{3/2}, \\
A^{\circ} &\equiv A(\gamma p \to \pi^{+} \Delta^{\circ}) = \sqrt{\frac{1}{6}} A_{1/2} - \sqrt{\frac{8}{15}} A_{3/2}.
\end{aligned}
\tag{VI-14}
$$

$A_{1/2}$ and $A_{3/2}$ correspond to s-channel isospin 1/2 and 3/2 amplitudes, respectively.

The amplitude H^{II} corresponding to s-channel nucleon-exchange vanishes in the Coulomb gauge in the c.m. system, and the amplitude H^{IV} corresponding to the Δ-exchange in the u-channel is very small, so that these two amplitudes can be ignored. According to the results of the partial wave analysis of single pion photoproduction, and the phase shift analyses of πN elastic scattering and $\pi N \to \pi\pi N$, the resonances having the isospin of 1/2 such as $P_{11}(1490)$, $D_{13}(1520)$, $D_{15}(1670)$, and $F_{15}(1788)$ have large photon coupling and large $\pi\Delta$ branching ratios. Taking into account of these facts and the discussion about R and R'' in section VI-3, $A_{3/2}$ amplitude was neglected.

Then the amplitudes of the three reactions can be expressed as follows;

$$T^{++} \equiv T(\gamma p \to \pi^- \Delta^{++}) = -(H^I + H^{III}) + \sqrt{\frac{1}{2}} A_{1/2},$$
$$T^{+} \equiv T(\gamma p \to \pi^\circ \Delta^{+}) = -\sqrt{\frac{1}{3}} A_{1/2}, \qquad \text{(VI-15)}$$
$$T^{\circ} \equiv T(\gamma p \to \pi^+ \Delta^{\circ}) = \sqrt{\frac{1}{3}}(H^I + H^{III}) + \sqrt{\frac{1}{6}} A_{1/2}.$$

Finally the cross sections of the three reactions are written down by using two parameters r and ϕ as follows;

$$\frac{d\sigma}{d\Omega^*}(\gamma p \to \pi^- \Delta^{++}) = \left(1 - \sqrt{2}\, r \cos\phi + \frac{r^2}{2}\right)(H^I + H^{III})^2, \qquad \text{(VI-16-a)}$$

$$\frac{d\sigma}{d\Omega^*}(\gamma p \to \pi^\circ \Delta^{+}) = \frac{1}{3} r^2 (H^I + H^{III})^2, \qquad \text{(VI-16-b)}$$

$$\frac{d\sigma}{d\Omega^*}(\gamma p \to \pi^+ \Delta^{\circ}) = \frac{1}{3}\left(1 + \sqrt{2}\, r \cos\phi + \frac{r^2}{2}\right)(H^I + H^{III})^2, \qquad \text{(VI-16-c)}$$

with

$$r = |A_{1/2}|/(H^I + H^{III}),$$
$$\phi = \arg A_{1/2}{}^{*)}, \qquad \text{(VI-17)}$$

where r represents the ratio of the absolute value of the $I_s = 1/2$ resonance amplitude to that of the Born amplitude. The parameters r and ϕ were evaluated using the present data and the calculated Born amplitudes. The results are shown in Fig. 50. A fairly large value of $r \sim 1$ was obtained in the second resonance region. This indicates that neither the pure GIOPE model nor the pure isobar model is a correct way to describe the reaction $\gamma p \to \pi \Delta$.

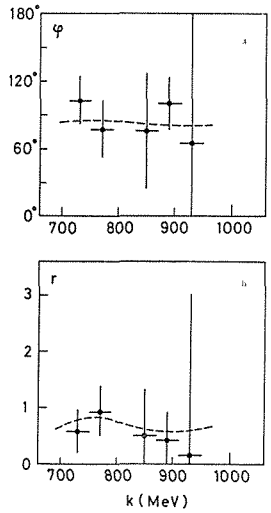

Figs. 50. Calculated values for (a) r and (b) ϕ. Dashed curves are obtained from the results of the analysis made by Sasaki.

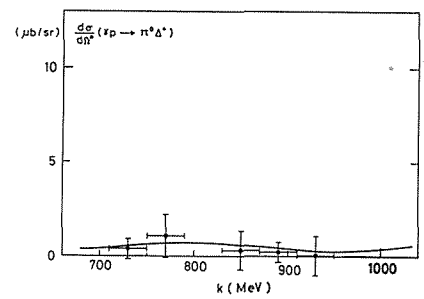

Fig. 51. Differential cross sections of $\gamma p \to \pi^\circ \Delta^+$ at a c.m. angle $\theta_\pi{}^* = 75° \pm 10°$. The solid curve represents the results of the analysis by Sasaki with $\lambda = 1.2$ GeV^{-2}.

*) The Born term has a pure real phase.

Since the reaction $\gamma p \to \pi^\circ \Delta^+$ has a negligibly small contribution from the electric Born term of H^{II} and H^{IV}, this reaction is sensitive to determine the resonance contribution. Because it is difficult to detect two neutral particle in the final state and the cross section is supposed to be rather small, no data are available up to now. The cross section at $\theta_{\pi^\circ}{}^* = 75^\circ \pm 10^\circ$ is evaluated from equation (VI–16–b) using the obtained value r. The values of $(H^I + H^{III})^2$ was evaluated with the absorption correction of formula (VI–8). The calculated cross sections are shown in Fig. 51 and are in agreement with the analysis by Sasaki.

VI-5. Conclusion

The following conclusions are obtained from the present experiment of double pion photoproduction from protons and the analysis on the quasi-two body reaction $\gamma p \to \pi \Delta$ in the photon energy range from 710 MeV to 950 MeV.

(1) The spectra of reactions (II–1),..., (II–7) can be explained well by the combination of the quasi-two body reaction and the phase space production.
(2) The quasi-two body reaction $\gamma p \to \pi \Delta$ is dominant in the double pion photoproduction process.
(3) The obtained ratio $R = 0.30 \pm 0.06$ at $\theta_\pi{}^* = 75^\circ \pm 10^\circ$ indicates the existence of the s-channel isospin 1/2 resonance contribution and/or GIOPE contribution to $\gamma p \to \pi^- \Delta^{++}$ and $\gamma p \to \pi^+ \Delta^\circ$.
(4) The observed ratio of the resonance amplitude to the GIOPE amplitude is equal to about 1 in the reaction $\gamma p \to \pi \Delta$ around the second resonance region.
(5) The cross sections of $\gamma p \to \pi^- \Delta^{++}$ and $\gamma p \to \pi^+ \Delta^\circ$ are reproduced by the sum of the amplitudes of the GIOPE model and the $I_s = 1/2$ resonances.
(6) From the behavior of the photon energy dependence of the laboratory cross sections of $\gamma p \to p \pi^\circ \pi^\circ$, the amplitude of the reaction is expected to be dominated by the s-channel resonances contribution in the second resonance region.

ACKNOWLEDGEMENTS

The author would like to express his sincere thanks to Prof. K. Miyake and Prof. S. Homma for their continuous encouragements and guidances throughout this work. He appreciates so much to Dr. H. Okuno for his excellent guidance in various stages of the experiment.

He is deeply grateful to Prof. A. Sasaki, Dr. N. Yamashita, Dr. H. Fujii, Dr. A. Itano, Mr. Y. Hoshi, Mr. I. Arai, Mr. H. Ikeda, Mr. T. Ishii, and Mr. E. Ohshima for the collaboration in carrying out this experiment. Especially he thanks to Prof. A. Sasaki, Dr. N. Yamashita, and Dr. H. Fujii for their helpful suggestions on the analysis.

He thanks also to Prof. T. Nakamura and Dr. K. Ukai for their useful advices in the course of this work.

He is much indebted to Prof. S. Yamaguchi, Prof. K. Huke, and the operating crew of the synchrotron for their skilful operations. The analysis of the data has been performed using the computer TOSBAC–3400 at the INS computer facility.

He thanks to Mrs. H. Katayama and Miss K. Sasajima for typing the present thesis and to Miss A. Sato for preparing clean drawings.

Appendix A. Wire spark chamber

(1) *Construction*

Although the seven planes of wire spark chambers used in this experiment had different dimensions as listed in Table 3, they had the same basic structure. Chamber frames made of epoxy glass (G–10) were 8 mm in thickness. The chamber was operated with low voltage because of a small gap. After the frames were polished smooth, 127 μm thick Mylar strips were attached to the edges of the active area in order to prevent edge breakdown. Wires made of stainless steel of 100 μm in diameter were laid down on the frame at an equal spacing of 1 mm under a constant tension of 300 g by a wire winding machine. Both ends of the wires were glued to the frame with Cemedine–1500, and one end was soldered to the copper tape bus. Then two planes of wired frame were covered with Mylar sheets of 127 μm thick for gas-seal. Each chamber had two planes of wires, the wires of one plane were set up at horizontal direction, and wires of the other plane were set up in the vertical direction or $\pm 10°$ from the vertical direction.

High voltage pulses for the chambers were generated in two steps. At first, a Kritron High Voltage pulser triggered by the master pulse generated the pulses of about 3 kV high, the pulse triggered a Thyratron High Voltage pulser. Then the high voltage pulse of 5.5 kV in amplitude and 60 nsec in rise time was fed to each chamber through a capacitor of 4000 pF. A clearing field of 100 V was supplied to each chamber having an opposite polarity to the high voltage pulse.

Gas mixture of 33% Neon and 67% Helium was supplied to each chamber with flow rate of 30 cc/min and 70 cc/min for WSC 1$\sim$4 and WSC5$\sim$7, respectively.

(2) *Readout system*

The magnetostrictive readout technique was used to readout the positions of the sparks in a chamber. Magnetostrictive lines, in which electrical currents of the sparked wires and the fiducial wires were transformed to elastic stress waves, were mounted on the frames of the chambers. The stress wave traversed from the position of the sparked wire and the fiducial wire to the end of the chamber with a propagation velocity of about 5.4×10^5 cm/sec. The pick-up coil with a cylindrical bias magnet placed at the end of chambers transformed the stress wave in the magnetostrictive line into an electrical signal. The signals were amplified and were fed to the spark position digitizing circuits via 50 Ω coaxial cable. The circuits digitized the time interval between the front fiducial signal and the succeeding spark signals in the following way. At first, the timing of the peaks of the signals were detected by a zero-crossing discriminator. This timing signal of the front fiducial signal opened the gate of a Clock Generator and generated the 20 MHz clock pulses which were fed into four scalers. The scaler continued to count the number of the clock pulses until the second timing pulse closed the gate of the first scaler. Thus the first scaler measured the time interval between the front fiducial signal and the first spark signal. Each succeeding timing signal turned off the scaler in the above manner. It was possible to digitize up to four spark positions by this digitizing equipment.

The contents of these scalers were read into a computer through CAMAC CCA and the branch driver by using a WSC Controller Module.

(3) *Performance*

Since the clock count of back fiducial wire corresponds to the time difference between the front fiducial wire and the back fiducial wire, this clock count was always used to calibrate the propagation velocity in the magnetostrictive line. The events which were associated with no back fiducial count or the edge sparking were excluded in the reconstruction procedure of spark positions. The average efficiency for proper spark events was 94%. The angular dependence of the spark efficiency was measured at injection angle from 10° to 40°, and was found to be constant.

The spatial resolution of the chamber was estimated with the distribution of deviations of the spark positions from the fitted straight line for three or four chambers. The resolutions were estimated to be ± 0.4 mm and ± 0.5 mm in the horizontal and in the vertical, respectively. The standard deviation of the fitting of the trajectory was given by the following formula,

$$\sigma = \sqrt{\sum_{i=1}^{n} (x_i' - x_i)^2/(n-2)},$$

where n is the number of the tracks used for the fitting, and x_i' and x_i are the position of the spark and the calculated position from the fitted trajectory, respectively. The distribution of σ in the case of four chambers was given in Fig. A–1.

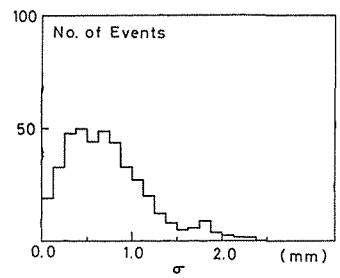

Fig. A–1. Distribution of the standard deviations of the linear fitting of four spark positions in the downstream of the magnetic spectrometer.

Appendix B. Calculation of the acceptance

The Monte Carlo calculation has been performed to evaluate the acceptance which is defined by equation (V–3) in Section (V–3). The program of the Monte Carlo calculation consisted of the following three steps.

(1) *Trajectory tracing*

The upstream trajectory in the spectrometer can be determined by $\boldsymbol{r}$, θ, and ϕ. Since we know the effective length of the magnetic field and the field strength, the trajectory in the magnetic field and the downstream trajectory are also determined from the momentum and the upstream trajectory. Particles are, however, deflected by the multiple Coulomb scattering, and lost their momentum by the ionization effect in the various materials, and a part of the particles are lost due to the decay and absorption by the materials in the spectrometer.

Taking account of the following conditions and effects, the particle trajectory

was traced step by step.

(a) Initial variables p, $\cos\theta$, and ϕ were so generated their distribution are uniform in their areas of integration. The distribution of the reaction points were assumed to be uniform in the beam direction and gaussian in the plane at right angle to the beam direction.

(b) If the trajectory passed through the triggering counters, the names of the counters were stored in the memories.

(c) If the trajectory did not pass through the magnet entrance and exit, the tracing was stopped.

(d) If the trajectory hit the side wall of the magnet, the tracing was also stopped.

(e) The coordinates having a gaussian distribution around the incident position of the trajectory at the chamber were stored as the spark positions.

(f) The momentum loss was calculated for each material by the formula given by Livingston and Bethe, and was subtracted from that of the incoming trajectory.

(g) The multiple Coulomb scattering was also considered. The distribution of the scattering angles was assumed to be gaussian.

(h) The $\pi \to \mu\nu$ decay were also taken into account in the calculation for the pion trajectory. The decayed muons were traced following the criteria.

By the above trajectory tracing, three names of triggering counters, seven coordinates of tracks in the wire spark chambers, and the initial and final p, θ, and ϕ were recorded as the simulated data for each event. They were damped on to the magnetic tape for the second step analysis.

(2) *Reconstruction*

In order to reconstruct the trajectory from the simulated data, we used the same program described in section IV–2. The momentum of the reconstructed events was calculated as in section IV–3. The events selection was also made following the procedure described in section IV–7.

(3) *Result*

The acceptance of the spectrometer was evaluated by using the number of the accepted trajectories N determined for each momentum bin and the number of the generated trajectories N_0. The solid angle of the spectrometer for a momentum interval from $p-\Delta p/2$ to $p+\Delta p/2$ can be expressed as follows;

$$\Delta\Omega(p) = \Omega_0 \frac{N(p)}{N_0(p)},$$

where Ω_0 denotes the solid angle for the generated trajectories.

These calculations were performed for pions and protons separately. The results are shown in Figs. 31–a and b.

The angular resolution of the spectrometer was also evaluated by this program and are shown in Figs. 31–c and d. The distribution of the deviations between the initial emission angles and the reconstructed ones gave the angular resolution of the upstream three wire spark chamber system. In the same way, the angular resolution of the downstream four chamber system was determined.

REFERENCES

1) For references and reviews, see; D. Lüke and P. Söding, Springer Tracts in Modern Physics **59** (1971) 39.
2) Cambridge Bubble Chamber Group, Phys. Rev. **155** (1967) 1477 and **163** (1967) 1510.
3) ABBHHM Collaboration, Phys. Rev. **175** (1968) 1669 and **188** (1969) 2060.
4) G. Gialanella et al., Nuovo Cimento **63A** (1969) 892.
5) J. V. Allaby, H. L. Lynch and D. M. Ritson, Phys. Rev. **142** (1966) 887.
6) M. G. Hauser, Phys. Rev. **160** (1967) 1215.
7) J. P. Burq et al., Nuovo Cimento **56A** (1968) 1142.
8) S. Fukui et al., Nucl. Phys. **B81** (1974) 378.
9) S. Costa et al., Nuovo Cimento **45A** (1966) 696.
10) M. Beneventano et al., Nuovo Cimento **15A** (1973) 449.
11) T. Kitagaki et al., J. Phys. Soc. Japan **42** (1976) 1083.
12) S. D. Drell, Rev. Mod. Phys. **33** (1961) 458.
13) P. Stichel and M. Scholz, Nuovo Cimento **34** (1964) 1381.
14) D. Lüke, M. Scheunert and P. Stichel, Nuovo Cimento **58A** (1968) 234.
15) G. Ciocchetti et al., Lett. Nuovo Cimento **1** (1969) 21.
16) D. Lüke, Thesis, University of Hamburg (1971), unpublished.
17) A. A. Zayats, Soviet J. of Nucl. Phys. **16** (1973) 597.
18) A. Sasaki, Thesis, Kyoto University (1974), Memoirs of the Faculty of Science, Kyoto University, **35** (1977) 1.
19) S. Arai et al., Japan. J. appl. Phys. **14** (1975) 95.
20) S. Homma et al., INS-TH-82 (1972).
21) M. M. Block, D. T. King and W. W. Wada, Phys. Rev. **96** (1954) 1627.
22) T. Kitami et al., INS-TH-94 (1975).
23) M. S. Livingston and H. A. Bethe, Rev. Mod. Phys. **9** (1937) 263 and on the density effect, see also; O. Halpern and H. Hall, Phys. Rev. **73** (1948) 477.
24) H. Fujii et al., Nucl. Phys. **B114** (1976) 477.
25) P. V. C. Hough, Phys. Rev. **74** (1948) 80.
26) I. Arai et al., J. Phys. Soc. Japan **43** (1977) 363.
27) J. D. Jackson, Nuovo Cimento **34** (1964) 1644.
28) J. Shapiro, Nuovo Cimento **18** (1960) 40.
29) S. D. Ecklund and R. L. Walker, Phys. Rev. **159** (1967) 1195.
30) R. G. Moorhouse, H. Overlack and A. H. Rosenfeld, Phys. Rev. **D9** (1974) 1.
31) J. S. Barton et al., Nucl. Phys. **B84** (1975) 449.
32) P. Dougan et al., LUDY (1975) 7502.
33) M. Yoshioka et al., INS-Report-281 (1977).